Bachelor Thesis

Damage Study on Single Strand Nb_3Sn

Ultra-Fast Beam Impact in Cryogenic Environment

Simulation with Finite Element Method

Jonathan Schubert

July 2020

Supervision Prof. Dr. Thomas Stöhlker
Dr. Daniel Wollmann

Abstract

At present, high energy physics requires high field magnets in large accelerators like CERN's LHC. In addition to the existing Nb-Ti magnets the upcoming HL-LHC will use Nb_3Sn based magnets for the first time in a high energy accelerator.

In specific failure cases, beams can impact the aperture of their accelerator. This causes ultra-fast local temperature gradients of several $100\,\mathrm{K\,mm^{-1}}$ in the superconducting magnets. The thermal stresses associated with such impacts can potentially damage the superconductors.

The scope of this study is to evaluate the superconductor damage limits in case of ultra fast, direct beam impact. To imitate the conditions in the accelerator an experiment was conducted at CERN's HiRadMat beam irradiation facility. The strands were cooled to $4\,\mathrm{K}$ and consequently impacted by 3×10^{12} $440\,\mathrm{GeV}$ protons over $600\,\mathrm{ns}$.

This thesis discusses the simulation model of the experiment. The model was set up with finite element software to improve the understanding of the observed degradation of critical parameters in Nb_3Sn strands. The main damage mechanisms were identified to be residual lattice strain in the superconducting phase, and filament cracking.
Following a brief overview of the impact experiment, the FEM simulation is described. Consequently, the implementation of the identified damage mechanisms in the post processing of the simulation data is explained. Lastly, the resulting superconductor properties are compared to post impact measurements. The comparison shows good agreement within the respective confidence intervals.

Zusammenfassung

Heutzutage werden für experimentelle Hochenergiephysik große Beschleunigeranlagen wie zum Beispiel CERNs LHC verwendet. Viele dieser Beschleuniger benötigen starke Magnete. Zusätzlich zu den Nb-Ti Magneten, welche bereits im LHC verbaut waren, werden in Folge des HL-LHC Projekts zum ersten Mal Nb_3Sn Magnete in einem Hochenergiebeschleuniger verwendet werden.

In speziellen Fehlerfällen kann der Strahl in einem Beschleuniger teilweise in dessen Apertur gelangen. Dies kann zu ultra-schnell auftretenden Temperaturgradienten von mehreren $100\,\mathrm{K\,mm^{-1}}$ in den supraleitenden Magneten führen. Der dadurch auftretende thermische Druck kann den Supraleiter beschädigen.

Die Studie zu der diese Arbeit gehört befasst sich mit den Schadensgrenzen im Falle einer ultra-schnellen direkten Deposition des Strahls in einen Magneten. Um einen solchen Fall für einen Magneten im LHC nachzustellen, wurde ein Experiment in CERNs Einrichtung für direkte Protonenbestrahlung (HiRadMat) durchgeführt. In diesem wurden einzelne Supraleiterdrähte auf 4 K gekühlt und dann mit 3×10^{12} 440 GeV Protonen über ein Zeitfenster von 600 ns beschossen.

Diese Arbeit soll die Simulation des Experimentes erläutern und diskutieren. Das Experiment wurde mit Finite Element Software nachempfunden, um die gemessene Degradierung kritischer Parameter der Nb_3Sn Drähte zu erklären. Als Hauptmechanismen der Degradation wurden eine residuelle Spannung in der supraleitenden Phase und das Brechen von Subfilamenten identifiziert.
Nach einem kurzen Überblick von Theorie und Experiment wird die FEM Simulation beschrieben. Die Implementierung dieser Mechansimen und die Nachbearbeitung der Daten aus der FEM Simulation werden vorgestellt. Schließlich werden die resultierenden Supraleitereigenschaften mit gemessenen Werten verglichen. Dieser Vergleich zeigt eine gute Übereinstimmung innerhalb der jeweilig zu erwartenden Varianzen.

Acknowledgements

First and foremost, I am extremely grateful to my CERN supervisors Daniel Wollmann and Andreas Will for granting me the opportunity to work on the project with them. Their continued support and feedback throughout my stay at CERN and afterwards cannot be overestimated. I am also deeply indebted to Thomas Stöhlker of the HI-Jena for supervising this thesis, which would not have been possible without him.

I would also like to thank my engineering friends and colleagues Carmelo Barbagallo, Lorenzo Bortot, and Michał Wilczek for helping me with understanding ANSYS® and FEM analysis in general in a reasonable amount of time. On this note, I would also like to thank my office mate Thomas Cartier Michaud for helping me with any code related question I could come up with.

I would like to extend my gratitude to the entire TE-MPE-PE section for the memorable time I was lucky to have there.

Thanks should also go to Carmine Senatore and Marco Bonura of the University of Geneva, who were always open to discuss the ideas we had about the study and how to measure them.

This work was made possible by CERN's Technical Student Programme and the HiLumi Project.

Finally, I would like to take this opportunity to thank my friends and family for their patience and love which I can always rely on. Especially concerning this thesis, I want to mention Maria Sadlik, Douglas Smith and Michał Wilczek. In particular, I would like to deeply thank my parents for their unconditional love and always backing me, no matter what.

Contents

1 Introduction

1.1 European Organisation for Nuclear Research and Large Hadron Collider

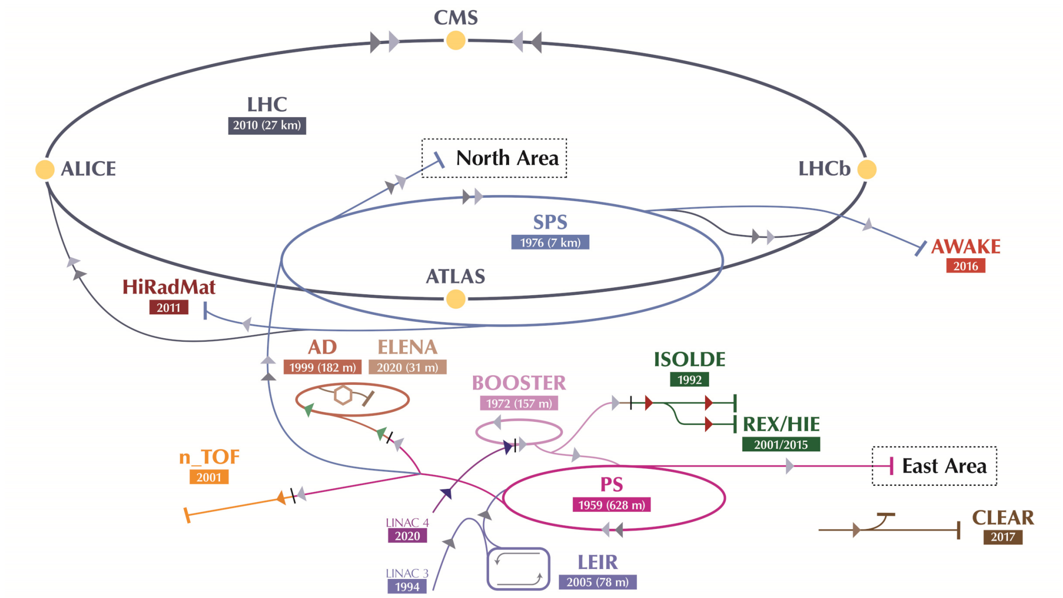

Figure 1.1: A schematic view of the CERN accelerator complex [1].

Founded in 1952 by twelve states, spanning across national boarders, and devoted to non-military research, the European Organisation for Nuclear Research (CERN) remains a testament to international collaboration and scientific pursuit to this day [2]. The laboratory is home to the worlds largest particle accelerator, the Large Hadron Collider (LHC). Along the 27 km long synchrotron, strong superconducting electromagnets guide the two proton beams which circulate along the ring in opposite directions. At four interaction points, the two beams collide within the LHC experiments ATLAS, ALICE, CMS and LHCb (see Fig.1.1). Here, the particle collisions result in energy densities high enough to generate exotic and elusive particles in quantities unparalleled anywhere else on the planet. Investigating these particles can help answer fundamental questions of physics and philosophy about the laws governing our universe.

1.2 Motivation of the study

The LHC was designed to collide particles at an unmatched energy level of up to 14 TeV in the centre of mass frame. To confine the two beams with an energy of currently 6.5 TeV (nominal 7.0 TeV) circulating along the 26.7 km circumference requires strong magnetic fields, which are provided by superconducting magnets. These magnets store large amounts of energy and can enter the normal conducting state due to small disturbances. Hence, highly sophisticated machine protection systems are required. The Machine Protection and Electrical Integrity group in CERN's Technology Department

(TE-MPE) is responsible for several of the LHC's machine protection systems. A large part of preventing failures are failure case studies, which usually focus on the magnet circuits and the beams.

At the time of this work, CERN's accelerator complex is in its second Long Shutdown(LS2), during which major maintenance works and upgrades are conducted. The main upgrade during LS2 include connecting the newly constructed LINAC4 to the Proton Synchrotron Booster, and the upgrades of all accelerators up to the LHC. This will make it possible to nearly double the LHC beam intensity in its High Luminosity era.

To unlock its full potential, the LHC will undergo its High-Luminosity upgrade in Long Shutdown 3 (2025/26). This will raise the integrated luminosity - a measure for the total number of collisions - until the LHC's end of life by a factor 10 (from $300\,\mathrm{fb}^{-1}$ to $3000\,\mathrm{fb}^{-1}$). To reach this goal, the final focusing magnets of ATLAS and CMS, among others which are currently based on Nb-Ti superconductors, will be replaced by novel Nb_3Sn magnets [3, 4].

These upgrades demanded studying the superconducting magnets' damage limits with respect to direct impact of the stored beam due to a fast failure. Thus, several damage experiments were performed to study a direct beam impact's effect on superconducting magnet components [5, 6]. The most recent experiment studied the damage caused by high energy protons on Nb-Ti and Nb_3Sn strand samples at $4.5\,\mathrm{K}$ and was performed in CERN's HiRadMat facility (see Fig.1.1). Thermo-mechanical simulations of the beam experiment were performed to better understand the observed damage in the strand samples and to identify the dominating damage mechanisms.

This thesis describes the different steps of the simulation and compares its results to the observed damage in the Nb_3Sn superconductor strands.

2 Theory Overview

This study is based on theories from different fields of physics and computer sciences. Introducing them in full depth is outside of this thesis' scope. However, the following sections will give a short introduction of the concerned subjects. Literature for further reading will be suggested if it is deemed necessary.

2.1 Particle Matter Interaction

This thesis will investigate the effects of the interaction between a high energy charged particle beam and a target. Therefore, it relies heavily on an accurate description of the particle-matter interactions(PMI). For this study the PMI will be computed with the Monte Carlo code FLUKA (see 3.1). To gain some understanding of the occurring processes, this section will briefly discuss the interaction of energetic hadrons with matter. A more complete introduction to PMI can be found in the 2018 CERN lecture by Lechner [7]. The standard nomenclature used in this section is taken from there, unless marked otherwise.

2.1.1 Cross Section and Mean Free Path

The interaction of a particle projectile with a target atom is quantified by its microscopic cross-section σ. The cross section is a function of particle energy, the atomic mass number A and the atomic number Z. In a target material, the mean free path for an incoming particle, i.e. the average distance between two successive collisions is given by

$$\lambda = \frac{1}{N\sigma} = \frac{M}{\rho N_{\mathrm{A}}\sigma} \quad , \tag{2.1}$$

with the atom density N, the molar mass M, the material's mass density ρ and the Avogadro constant N_{A}.

Let a particle be normally incident in a homogeneous material, where the mean free path is λ. Then the probability of the particle to interact between a penetration depth l and $l + \mathrm{d}l$, is then given by

$$p(l)\mathrm{d}l = \frac{1}{\lambda}\exp\left(-\frac{l}{\lambda}\right)\mathrm{d}l \quad . \tag{2.2}$$

Thus, the probability of the particle to have interacted at a penetration depth l is given by the cumulative density function

$$P(l) = \int_0^l p(l')\mathrm{d}l' = 1 - \exp\left(-\frac{l}{\lambda}\right) \quad . \tag{2.3}$$

2.1.2 Atomic Interactions of Charged Hadrons

Charged particles travelling past the nuclei and electrons of matter are subject to Coulomb interaction. This changes their initial trajectory and, in turn, alters the material itself.

Interaction with electrons usually leads to an excitation or ionisation of the atom. Interactions with nuclei mainly affect the angular deflection of the charged particle. Therefore, the change of particle energy per path length is dominated by the electron system up to a certain threshold particle energy, beyond which radiative effects become more important. This stopping power is defined by

$$\left(\frac{\mathrm{d}E}{\mathrm{d}x}\right)_{\mathrm{elec}} = N \int_0^{T_{\max}} T \frac{\mathrm{d}\sigma}{\mathrm{d}T} \mathrm{d}T \quad [8], \tag{2.4}$$

where $\frac{\mathrm{d}\sigma}{\mathrm{d}T}(T)$ is the differential cross section, and T is the energy transferred to an electron. The electronic energy loss heats up the material.

Lighter particles scatter more than heavy particles at the same $\beta\gamma$. Thus, the energy loss for electrons above $\sim$10 MeV will be dominated by radiating bremsstrahlung. The heavier protons, on the other hand, will only experience significant losses through this mechanism at much higher energies in the order of $\sim$100 GeV [7].

Above energies of $\sim$1 MeV the Bethe equation

$$-\left\langle\frac{\mathrm{d}E}{\mathrm{d}x}\right\rangle = \frac{4\pi n_{\mathrm{e}} z^2}{m_{\mathrm{e}} c^2 \beta^2} \cdot \left(\frac{e^2}{4\pi\varepsilon_0}\right)^2 \cdot \left[\ln\left(\frac{2 m_{\mathrm{e}} c^2 \beta^2}{I \cdot (1-\beta^2)}\right) - \beta^2\right] \quad [8] \tag{2.5}$$

describes the electronic energy loss dE per penetration depth dx. Here, the charge of the particle (in multiples of a positron charge e) z, and the particle velocity β in natural units, are particle properties. The electron density n_{e}, and mean excitation potential I are material properties. Above a given threshold, radiative losses add a linear $\beta\gamma$ dependence to the stopping power. The electron mass m_{e}, and the speed of light c are constants. For lower energies, the stopping power is mostly estimated with empirical formulas (eg. [9]).

2.1.3 Hadronic Nuclear Interaction

Hadron nucleus collisions are governed by the strong force. They are considered elastic if only the trajectories change, and inelastic if the internal structure of the hadron or the nucleus is changed.

During the first instances ($\sim 10^{-22}$ s) of the interaction new particles can be produced, provided that the incident particle energy is high enough[1]. The highly energetic hadrons can then leave the nucleus (mainly in forward direction) and form intranuclear cascades. Lower energy particles can excite the nucleus. In the following de-excitation-, or

[1] For interactions with a free nucleon, the incident particle energy needs to be at least 290 MeV, for nuclei this threshold energy can be smaller. Particle production becomes particularly important in and above the GeV range.

evaporation-phase ($\sim 10^{-16}$ s), lower energy particles (hadrons, γs, or even α-particles) are emitted isotropically. In heavy elements, fission can also occur during this phase, the products of which can enter evaporation as well [7, 10].

Above a certain energy threshold[2], inelastic scattering becomes the dominant mechanism. The mean free path due to inelastic scattering, is often referred to as the inelastic scattering length. It shows a material dependence of

$$\lambda \propto \frac{A^{\frac{1}{3}}}{\rho} \quad , \tag{2.6}$$

where A and ρ respectively represent the atomic mass number and the mass density. The dependence shows, that more densely, but also more equally distributed nucleons in the material favour this interaction. The inelastic scattering length in a material is usually larger than the radiation length of electrons. Therefore, hadronic showers are usually longer than their electronic counterparts.

2.1.4 Energy Deposition

The energy deposition of a beam in a given volume of matter is not necessarily equal to the energy the beam lost in the same volume. This is due to the fact, that possible δ-rays and secondary particles leaving the volume carry energy as well. From the conservation of energy one can determine, that the difference between the energy going into the volume and the energy coming out must be the deposited energy. This simple approach is no longer valid, when nuclear binding energies play a role.

In order to better compare the energy deposition profiles of different incident particles, it is practical to define the energy deposition parameter [7]

$$\varepsilon(z_{\mathrm{i}}) = \frac{1}{E_0} \frac{\Delta E(z_{\mathrm{i}})}{\Delta z} \quad . \tag{2.7}$$

This allows to qualitatively compare the fraction of energy ΔE deposited in the volume between z and $z + \Delta z$ for different initial particle energies E_0.

A hadron's energy deposition exhibits a characteristic Bragg peak if the initial energy is underneath the cascade induction threshold. This can be seen from the Bethe equation (Eqn.(2.5)), which shows that the stopping power increases significantly at the end of their penetration range. As Fig.2.1 shows, the final shape of the Bragg peak depends on the properties of the target material. For a beam of multiple particles, the shape of the peak is also determined by the beam parameters, such as the radial beam cross section. In the logarithmic representation of Fig.2.1, there are tails visible. These are due to secondary neutrons which carry energy far deeper into the material than the Bragg peak.

[2]For a proton-proton collision this would be in the order of $\sim$1 GeV.

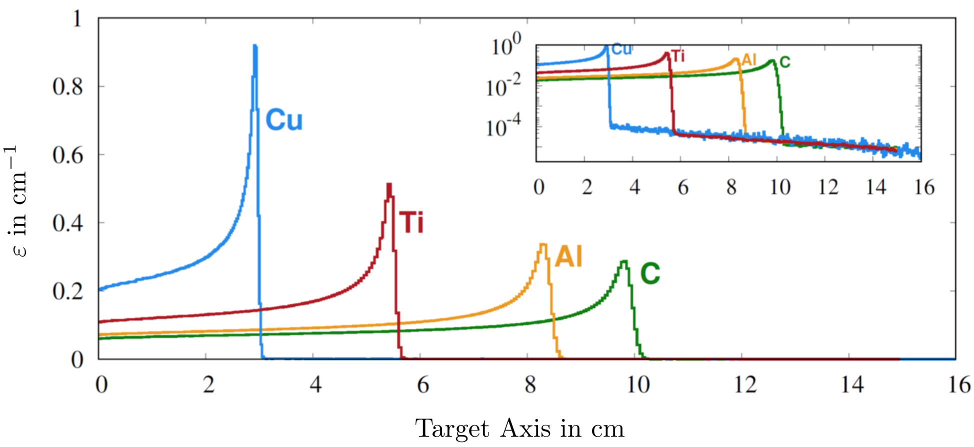

Figure 2.1: Energy depositions of a 160 MeV proton with a radially infinite slab of material. Normalised by Eqn.(2.7). The depositions are given for different materials exhibiting different shapes of Bragg peaks. This is an altered plot taken from Lechner's 2018 CERN lecture [7].

2.2 High Energy Hadronic Showers

For high energy primary hadrons, the energy deposition behaviour changes. This is shown in Fig.2.2, where for low initial energies a Bragg peak is prominent. For higher initial energies, the initial energy deposition is overshadowed by the shower and the energy distribution curve smooths out. If the primary hadron energy is high enough, inelastic collisions between the primary hadron and a target material nucleus will occur. The resulting collision products are referred to as secondary particles. If the forward secondary particle energy is still high enough, those particles will be subject to inelastic collisions themselves. This particle multiplication will continue until the particle energies fall below the production threshold[3]. The resulting cascade of particle multiplication is called a hadronic shower.

The deposited energy is now translated into heat in the material by interactions of lower-energy particles with the electronic system. A significant fraction of these lower-energy particles result from evaporation, gamma de-excitation and fission (see 2.1.3) in the impacted nuclei. Non-negligible parts of the initial energy will dissipate in the breaking of binding energies. The final shape of a hadronic shower is determined mainly by the inelastic scattering length in the material. The depth of the maximum energy deposition in the material scales more or less logarithmically with the initial primary particle energy, which can also be observed in Fig.2.2.

Due to the fact that some decays of particles in the shower will yield γ-particle pairs, hadronic showers also have an electromagnetic component. These components are much shorter than the hadronic components, because typically the radiation lengths of a material are smaller than the inelastic scattering length. With a higher particle energy, the induction of an electromagnetic shower becomes more likely. Therefore, electromagnetic showers are more common in the high energy radial centre of the hadronic showers. At

[3]This mainly refers to the production of pions.

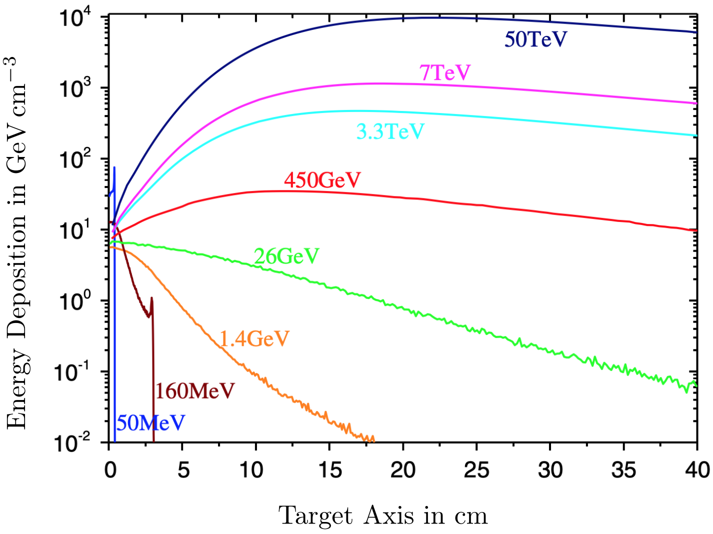

Figure 2.2: Energy deposition in solid copper for incident protons of given energy as simulated with FLUKA. The data shows a pronounced Bragg peak for the 50 MeV particle. From 1.4 GeV onward, the Bragg peak is covered by high energy effects. The plot is taken from [11].

very high energies the electromagnetic showers become the dominant mechanism in energy dissipation. For a 100 GeV proton, for example, about half of the dissipated energy is due to electromagnetic showers [7].

The transverse momentum of secondary particles of inelastic nuclear collisions shows little dependence on the initial energy [10]. Thus, the opening angle of the shower decreases with growing initial energy. This aligns the hadronic showers with the electromagnetic showers in the core of the hadronic shower, resulting in a very narrow shower profile.

2.3 Superconductivity

A major part of this thesis will be about correlating mechanical effects in a superconductor with its superconducting properties. This section will give a brief overview of general properties of superconductors. The properties discussed are applicable for Low Temperature Superconductors. The more recently discovered High Temperature Superconductors exhibit similar properties, but have to be motivated differently. This will be followed by a short introduction of the subject of this study: Nb_3Sn in RRP® strands, and its damage mechanisms.

2.3.1 Basics of Theory

Since it's discovery in 1911, superconductivity has been a field of extensive study in the physics community. Commonly, superconductors are known to exhibit resistance free electric conductivity below a critical temperature T_c. Superconductivity has been verified by experiments on currents induced into conductor rings, where the current decay times were in the order of 10^5 years [12].

Due to several effects superconductors in magnetic fields develop some small levels of resistivity[4]. This behaviour causes the resistivity of a technical superconductor to be a function of the current density. It can be described as

$$\rho(J) = \rho_\mathrm{c} \left(\frac{J}{J_\mathrm{c}} \right)^n \quad , \tag{2.8}$$

with the current density J, and the measurable critical current density J_c. The resistivity threshold ρ_c is conventionally chosen as $10^{-14}\,\Omega\,\mathrm{m}$. This definition implies quasi perfect conductivity, because a resistivity below $10^{-14}\,\Omega\,\mathrm{m}$ is practically not measurable. The quality value n is typically in the order of 10 for a technical superconductor, indicating a sharp transition in resistivity.

Superconductors can be categorised into two types. Type I superconductors behave like almost perfect diamagnets, which means that they repel an external magnetic field B_app. Shielding currents generate a magnetic field opposing the external field. This leads to a strong decay of magnetic field strength towards the centre of the conductor. This diamagnetism can only be sustained until a critical magnetic flux density B_c is reached. Above this limit the superconducting state collapses.

Type 2 superconductors, on the other hand, enter an intermediate regime above B_c. For these materials, it is energetically more stable to allow quantised magnetic flux vortices to penetrate the superconductor instead of switching into their normal conducting state. When reaching a second critical flux density B_c2 the superconducting state of a type II superconductor collapses as well and it enters into its normal conducting state. This limit is reached, when the energy density G of the penetrating magnetic field becomes larger than the difference between the energy density in the normal conducting state G_n and the energy density at the first critical magnetic flux density $G_\mathrm{s}(B_\mathrm{c})$, the superconducting state collapses.

The critical current density J_c of a superconductor is a function of temperature T and applied magnetic flux density B_app. This dependency can be described as a critical surface. Fig.2.3 shows the critical surface of a $\mathrm{Nb_3Sn}$ superconductor normalised to the critical Temperature T_c, the second critical magnetic flux density B_c2 and the critical current density J_c. Below this surface the superconductor is in its superconducting state and above this surface in its normal conducting state.

The superconducting magnets in the LHC are made from Nb-Ti, a very robust alloy. The HL-LHC aims to increase the luminosity[5] of the machine. This can be achieved by increasing the density of particles at the interaction points. Partly, this will be done by increasing the focusing, reducing the radial beam size at the interaction point by a factor of 2. To accomplish this goal at the same peak magnetic fields, the aperture of the focusing Magnets (Quadrupole Triplet) would have to be increased by a factor of 2 as

[4] A satisfying description of these effects would be too lengthy here, but can be found in common literature on the subject (e.g. Tinkham [13]).

[5] The luminosity is a measure of occurring collisions in a collider per unit time.

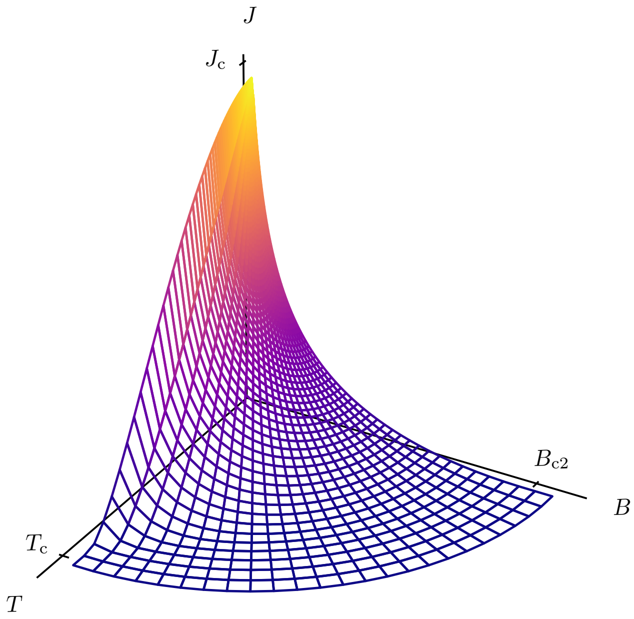

Figure 2.3: The critical surface of a Nb_3Sn superconductor normalised to the critical Temperature T_c, the second critical magnetic flux density B_{c2} and the critical current density J_c.

well. Nb-Ti is limited to peak magnetic field strengths of around 8 T, whereas Nb_3Sn can operate at ∼15 T. This allows for higher gradients in the focusing magnet reducing the need for an increase in aperture. Additionally, the Nb_3Sn magnets are shorter making space for other instrumentation in a crucial part of the machine [3].

For circular particle accelerators the achievable particle momentum scales with $B \times r$, where B is the magnetic flux density in the bending magnets and r is the effective radius of the accelerator. Thus, to reach higher particle momenta one can either increase the radius of the accelerator or increase the magnetic flux density on the bending magnets. Therefore, a high magnetic field tolerance is a direct criterion for superconductor candidates to be used in high energy accelerator magnets. This makes Nb_3Sn a valid option for future accelerators.

2.3.2 Technical Superconductor: Nb_3Sn

Discovered in 1961, Nb_3Sn was the first superconductor, which could be used in fields, above 10 T [14]. This opened up the possibility of different ambitious projects like ITER or the HL-LHC, which strongly rely on high field superconducting magnets. Nb_3Sn is an intermetallic compound of Nb and Sn which is formed in a complex heat treatment procedure taking several days. After the reaction Nb_3Sn is brittle and therefore the magnets have to be wound with un-reacted strands, reacted as a whole and then potted with epoxy resin to stabilise the strands. The strand geometries as well as the details of the heat treatment are directly effecting the critical parameters of the Nb_3Sn magnets and have therefore been optimised for different applications. For the HL-LHC, two types of strands with similar performance have been developed: the RRP (Rod-Restacked Process) strand, developed bu Oxford Instruments and the PIT (Powder in Tube) strand developed by Bruker. As the latter was significantly more expensive the RRP strand has become the one used for the majority of the HL-LHC high field magnets. Fig.2.4 shows the cross section of this type of strand. The RRP strand guarantees a minimum strand current density J_c of $2560\,\mathrm{A\,mm^{-1}}$ at 12 T and 4.2 K, and a residual resistance ratio[6] (RRR) in the copper greater than 150 [4].

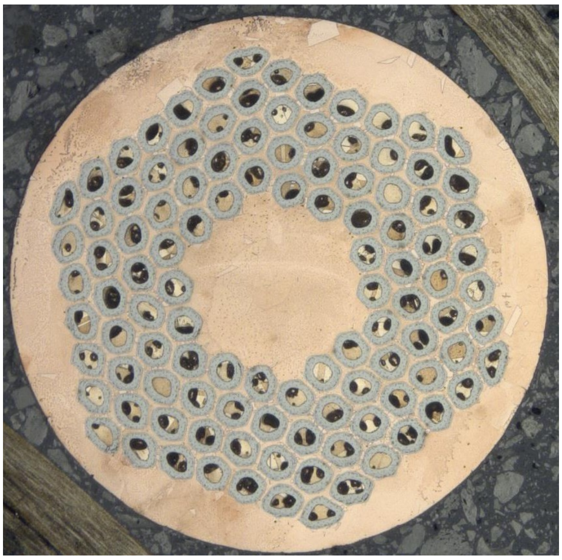

Figure 2.4: Cross section of RRP® 108127 strand used for the final focusing triplet quadrupoles for the HL-LHC; Courtesy of Mickael Meyer, EN-NME-MM, CERN

The magnetic flux density dependence of superconductor properties are often highly non-linear. Additionally, measuring them for type two superconductors can be challenging because of the high field strengths required. In order to make extrapolations of such superconductor properties more robust, it is common to represent them in a linearised form. This convention was introduced by Edward J. Kramer, who found a linear representation of the pinning force in dependence on the magnetic flux density [15]. Consequently, such linearisations are commonly referred to as Kramer form or Kramer representation. The critical current I_c as a function of the applied magnetic flux density B[7] is linearised by

$$f_{\mathrm{kramer}}(B) = I_c^{0.5} B^{0.25} \quad [16]. \tag{2.9}$$

The concept of the critical surface can be extended by including a strain dependence of the critical parameters. The local critical current density J_c depends, thus, on the magnetic flux density B, the temperature T and superconducting phase strain state ε. The dependence commonly found in literature (see [16]) is given by:

$$J_c(B, T, \varepsilon) = C(1 - t^2)b^{-0.5}(1 - b)^2 \tag{2.10}$$

[6] This parameter is usually defined as $\rho_{\mathrm{Cu}}(293\,\mathrm{K})/\rho_{\mathrm{Cu}}(4.2\,\mathrm{K})$ and gives an indication of the thermal stability of a strand. For superconductors, T_c is usually used as a cryogenic reference temperature instead of 4.2 K, so that a resistivity can be measured.

[7] In this thesis B will refer to the projection of $\vec{B}$ onto the plane orthogonal to the current $\vec{J}$.

$$B_{c2}(T,\varepsilon) = B_{c2,0}s(\varepsilon)(1-t^{1.52}) \tag{2.11}$$

$$T_c(\varepsilon) = T_{c,0}s(\varepsilon)^{1/3} \tag{2.12}$$

Here, C is a scaling constant depending on the specific strand type[8]. Furthermore, is $b = B/B_{c2}(T,\varepsilon)$, $t = T/T_c(\varepsilon)$ and $s(\varepsilon)$ a scaling function of ε. This formulation is divergent towards $B \to 0$, but deemed accurate above 1 T [16].

The scaling function, $s(\varepsilon)$, used in this paper was first proposed by Goedeke et al. [17] and is commonly referred to as Twente strain function or MAG-scaling(Mentink-Arbelaez-Goedeke). The formulation is given by

$$\begin{gathered} s(\varepsilon_a) = \frac{1}{1 - C_{al}\varepsilon_{0,a}}\left(C_{al}\left(\sqrt{(\varepsilon_{sh})^2 + (\varepsilon_{0,a})^2} - \sqrt{(\varepsilon_a - \varepsilon_{sh})^2 + (\varepsilon_{0,a})^2}\right) - C_{a2}\varepsilon_a\right) + 1 \quad , \\ \text{where } \varepsilon_{sh} = \frac{C_{a2}\varepsilon_{0,a}}{\sqrt{(C_{a1})^2 - (C_{a2})^2}} \quad , \\ \text{and } \varepsilon_a = \varepsilon_{applied} + \varepsilon_m \quad . \end{gathered} \tag{2.13}$$

Here, ε_a is the asymmetric deviatoric strain[9] in the superconductor. The other variables are empirical constants wich are given for the RRP strand used in this study in Tab.2.1.

Table 2.1: RRP 108/127 strain scaling constants according to Nijhuis [18] for a prestrain of $\varepsilon_m = 0.1\,\%$ [19].

C_{al}	C_{a2}	$\varepsilon_{0,a}$
59.36	23.91	3.09×10^{-3}

Based on axial strain measurements it is well documented in literature, that Nb_3Sn strands do not to return to their original $\varepsilon_{ax} = 0$ value after the unloading process (see [20]). This plastic deformation regime observed in strands is interesting, because solid Nb_3Sn is a brittle material, which breaks before reaching the plastic deformation regime. Cheggour et al. report an Irreversibility Cliff ε_{irr} [21], beyond which a further loading of the strand leads to a discrepancy between the loaded and unloaded $I_c(\varepsilon)$. However, the mechanism of this strand degradation is not explained in the paper.

As seen in Fig.2.4 the Nb_3Sn filaments are surrounded by a copper matrix, which is a ductile material. Therefore, it seems to be logical, that the plastic deformation of the surrounding ductile materials(in case of RRP®this is mainly copper) under strain will lead to a residual strain on the Nb_3Sn filaments. The exact correlation however is not as simple, as the filaments are twisted with with twist pitch of ∼19 mm [22].

[8] As we will see in 5.4.4 the exact value of C does not matter in the scope of this work, since it will be multiplied with an independent scaling constant.

[9] This is roughly equivalent to the volume preserving rotational shape change of the material.

Additionally, the fracturing of some Nb_3Sn filaments has to be taken into account. This is due to the fact that Nb_3Sn is a brittle material. Fracture of a subfilament reduces the overall I_c of the strand because the crack interrupts the superconducting phase. Apart from a few attempts (eg. [23]), the direct correlation between the fracture of subfilaments and a reduction of I_c is not very well documented in literature.

3 Simulation Tools

The simulation of the beam impact and the consequent effects in the samples and sample holder relies on commonly used simulation tools. In this chapter, the concept that the software relies on will be briefly discussed, after which the specific software will be introduced.

3.1 Monte Carlo Code: FLUKA

The simulation of the statistical energy distribution caused by the beam in the samples and sample holder was performed with the multi purpose particle simulation software FLUKA. The used FLUKA package relies on the Monte Carlo method.

3.1.1 The Idea of the Monte Carlo Method

The Monte Carlo method is a commonly relied on tool to solve multidimensional statistical problems. A mathematical introduction, as presented by Caflisch [24] is given in Appx.B.

In principle, the concept states that if a statistical problem is sampled, the yielded average result converges towards the expectation value of the problem for a growing sample number. This idea can be applied to statistical simulations. Here, it yields the fact, that if the simulation is run N times, with unbiased starting conditions, and N becomes large enough, the statistical simulation error decreases with $O\left(N^{-1/2}\right)$.

3.1.2 Overview of FLUKA

FLUKA is a multi purpose tool for simulations of particle transport and particle interaction with matter. It was originally developed by a collaboration of CERN and the Istituto Nazionale di Fisica Nucleare (INFN). The particle matter interaction package relies on statistical physics models in combination with a Monte Carlo code. The implemented microscopic models have been cross checked for consistency and validated with experimental data, as far as possible. Furthermore, conservation laws are enforced in each step. Therefore, FLUKA simulates the interaction and shower propagation of about 60 different particles with high accuracy up to energies of several TeV [25].

Geometries in FLUKA rely on Combinational Geometry (CG). FLUKA includes a set of predefined materials, but can be extended by providing their atomic composition and mass/volume fractions. The energy ranges FLUKA can cover go from 1 keV to multiple 1000 TeV for electrons and photons. For hadrons, muons and neutrinos, energies up to 20 TeV can be simulated reliably. Linking FLUKA with DPMJET can push this number up to 10 PeV [25, 26, 27].

3.2 Finite Element Method: ANSYS

The samples' and sample holder's thermal and mechanical response (see 5.2 and 5.3) to the beam impact was simulated using different packages in ANSYS®. These packages rely on the Finite Element Method.

3.2.1 Principles of the Finite Element Method

Physics experiments usually try to isolate certain phenomena in order to study them and give a mathematically accurate, and, where possible, analytical description. In reality, systems are often very complex and while the different contributors to this complexity might be understood by themselves, the combined outcome is difficult to predict. For this reason, discrete computer based simulation tools have become irreplaceable for a wide range of problems in industry and research alike.

One of the major approaches to discretisation is the Finite Element Method(FEM). In this approach, it is assumed that the problem can be described by a set of partial differential equations in a given domain. This domain is then discretised locally using simple elements (finite elements). The ensemble of these elements is referred to as the mesh. At specified points of the element (nodes) a load is applied. A set of matrix equations can then relate the local load to a reaction in nodes regionally. Combining the local sets of the elements' matrix equations, a global equation is formulated. Since this represents a set of linear equations, they can be solved by standard techniques to yield the output.

This static method can be extended with a finite difference method regarding discrete time steps into a transient evolution of a given problem. Here, to calculate the solution of the $i + 1$th step, the output calculated in the ith step is applied as a load. The standard literature example of this is the simulation of thermal diffusion. This example and other more complicated applications of FEM are well presented by Bergheau and Fortunier [28].

3.2.2 ANSYS® Software

ANSYS® Inc. is an American public company, which was founded in 1970 with the intent to automate the Finite Element Method. With its different software branches it covers a wide range of applications from simulating semi conductors to fluid interactions. For this work the ANSYS® Workbench module (product version 2019 R1) was used. It is a platform linking different modellers and simulation packages.

3.2.3 Strain Modelling in ANSYS® Mechanical

To clearly define the parameters taken from the simulations, the respective formulations will be given here. They are taken from the ANSYS® 2009 manual [29][10]. In this subsection, bold variables will represent matrices.

The thermal strain is derived by introducing the thermal expansion coefficient

$$\alpha = \frac{1}{l}\frac{\mathrm{d}l}{\mathrm{d}T} \quad , \tag{3.1}$$

with the current length l, and the temperature T. The thermal strain corresponds to the logarithmic strain defined by

$$\varepsilon_{\mathrm{log}} = ln\left(\frac{l}{l_0}\right) \tag{3.2}$$

(here, l_0 is the initial length), through

$$\varepsilon_{\mathrm{log}} - \varepsilon_{\mathrm{log,0}} = \alpha(T - T_0) \quad , \tag{3.3}$$

where $\varepsilon_{\mathrm{log,0}}$ is the initial strain and T_0 represents the initial temperature.

Equivalent plastic strain is computed incrementally by the following algorithm

1. The yield strength is determined for the current temperature.
2. The stresses are computed based on a trial strain

$$\boldsymbol{\varepsilon}_{\mathrm{tr,n}} = \boldsymbol{\varepsilon}_{\mathrm{n}} - \boldsymbol{\varepsilon}_{\mathrm{pl,n-1}} \quad , \tag{3.4}$$

   where $\boldsymbol{\varepsilon}_{\mathrm{pl,n-1}}$ is the plastic strain of the previous time step
3. If the computed equivalent stress is lower than the yield strength, the algorithm stops here, else it continues.
4. The plastic strain increment $\Delta\boldsymbol{\varepsilon}_{\mathrm{pl,n}}$ is calculated.
5. The current plastic strain is updated as

$$\boldsymbol{\varepsilon}_{\mathrm{pl,n}} = \boldsymbol{\varepsilon}_{\mathrm{pl,n-1}} + \Delta\boldsymbol{\varepsilon}_{\mathrm{pl,n}} \tag{3.5}$$

   and the elastic strain is computed by

$$\boldsymbol{\varepsilon}_{\mathrm{el,n}} = \boldsymbol{\varepsilon}_{\mathrm{tr,n}} - \Delta\boldsymbol{\varepsilon}_{\mathrm{pl,n}} \quad . \tag{3.6}$$

The total strain is defined by

$$\boldsymbol{\varepsilon}_{\mathrm{tot}} = \boldsymbol{\varepsilon}_{\mathrm{el}} + \boldsymbol{\varepsilon}_{\mathrm{pl}} + \boldsymbol{\varepsilon}_{\mathrm{cr}} \quad , \tag{3.7}$$

with the elastic strain $\boldsymbol{\varepsilon}_{\mathrm{el}}$, the plastic strain $\boldsymbol{\varepsilon}_{\mathrm{pl}}$, and the creep strain $\boldsymbol{\varepsilon}_{\mathrm{cr}}$. In the timescales of the experiment, no creep strain is expected to happen. Hence, the total strain reduces to the sum of plastic and elastic strain.

[10] This version was used, because ANSYS® discontinued user manuals afterwards. It is, however, reasonable to assume, that the formulation of these basic parameters has not changed since.

4 Experimental Procedures

The beam experiment and its results are at the basis to this work. Therefore, they are briefly described in the following. For further reading, please find the internal note regarding the experiment [30], the published results [6, 31], and the to be published study summary [32].

4.1 Beam experiment

In this section a short overview of the actual impact experiment is given as a motivation and model for the simulation. For a full overview of and motivation for the experiment find [30, 32].

4.1.1 Target Geometry

The main idea of the experiment was to expose Nb_3Sn, Nb-Ti strands and HTS tapes to high energy particles, causing localised thermal hotspots. The samples were fixed in a copper sample holder, which was also used to create hadronic showers along the beam axis and therefore expose samples installed further downstream to higher levels of energy deposition. In the sample holder, the samples were ordered in batches. Fig. 4.1 shows the sample holder. The strand positions are indicated by red dots and labelled. The sample holder is made from copper plates of different thickness, which are embedded between two steel plates and compressed together with two steel bolts.

Each batch of 10 samples was exposed to one single shot of 440 GeV protons. The energy deposition increases the further the beam penetrates through the sample holder and the samples (as described in 2.2). This is shown in Fig.4.2. Based on the energy deposition derived by FLUKA the hotspot temperature was calculated for each sample using the heat capacity of copper. The samples of each batch were arranged perpendicularly along the beam axis in such a way to achieve regular intervals of increasing hot-spot temperature.

To reproduce the cryogenic environment in which the superconducting magnets are operated in the LHC the sample holder was placed in a cryostat cooled by a cryogen free cryo-cooler[11] (see Fig.A.2). To avoid the use of beam windows and keep the unnecessary activation of materials as low as possible, the walls of the cryostat were made from the low Z material Aluminium. Therefore, the interaction of protons with the cryostat walls was small compared to the one with the actual target. Nevertheless, the FLUKA model used for the energy deposition calculations includes the cryostat walls.

[11] Note that the magnets in the LHC are operated at 1.9 K. The experiment, however, was performed at 4.5 K. As the thermal expansion and the heat capacity are very small between 1.9 and 4.5 K this setup reproduces the thermal shocks strands would experience in the LHC magnets reasonably well.

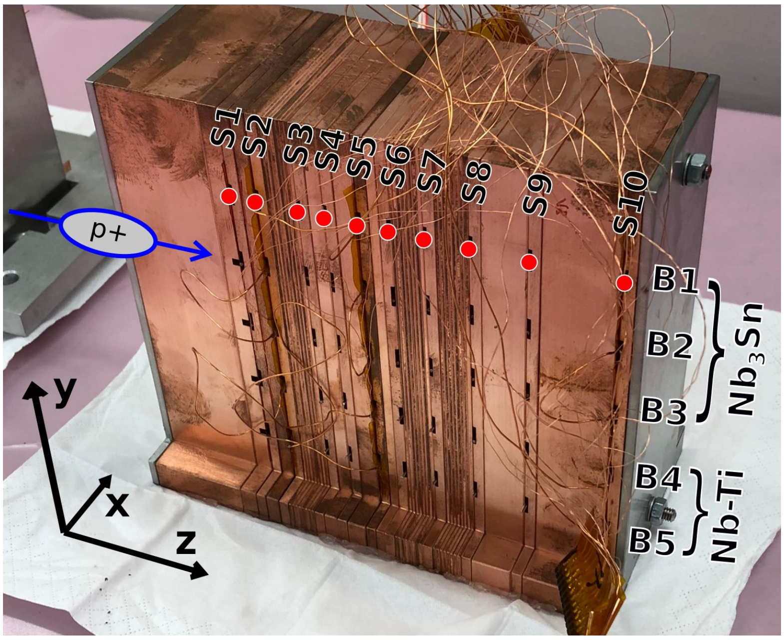

Figure 4.1: Sample holder of the sc. magnet component damage experiment with beam. The samples are placed in the grooves as indicated by the red dots. The batches consist of 10 samples of the same superconductor type each, where batches B1 to B3 are Nb_3Sn based and B4 to B5 are based on Nb-Ti. The beam direction is indicated by the blue arrow. The thin wires visible in the photo are instrumentation wires, which were intended for in-situ measurements during the experiment. Courtesy of Andreas Will, TE-MPE-TE, CERN.

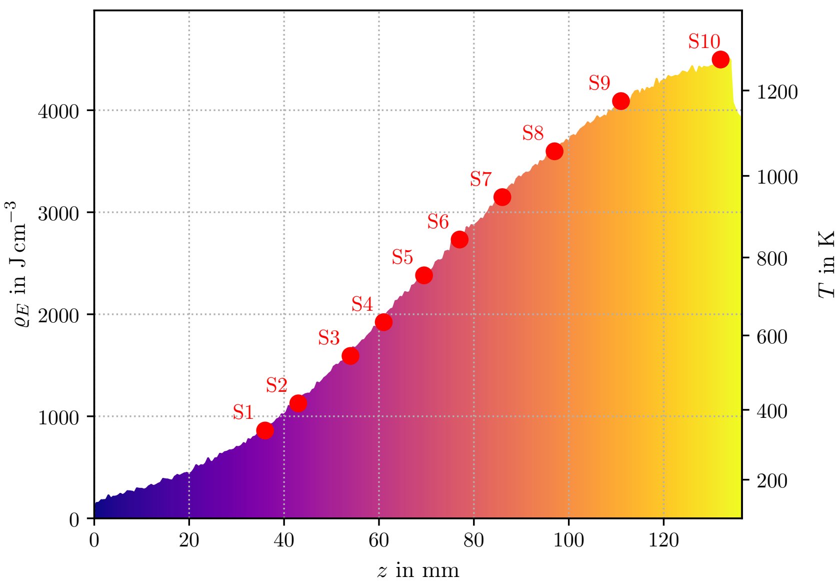

Figure 4.2: Expected energy deposition of binning cells along the beam axis including Strand locations. Corresponding temperature calculated for homogeneously, instantaneously heated copper-cell with a size of $1\,\text{cm}^3$.

4.1.2 Beam Impact Data

In the irradiation facility, the beam parameters (transverse beam size, shot intensity and beam position) vary slightly from shot-to-shot. To maximise the reproducibility, the beam intensity was kept constant from shot to shot.

After the experiment, the beam impact position for each batch of samples was derived by measuring the beam imprint marks in the sample holder. From this the discrepancy between the vertical beam impact position and the centre of the strands was calculated. For Batch B1, B2 and B3 these offsets were 1.2 mm, 1.0 mm, and 1.1 mm [30]. The simulations shown in this thesis were performed with a vertical offset of 1.1 mm.

The measured beam intensities for batches B1, B2 and B3 were 3.08×10^{12}, 3.07×10^{12}, and 3.09×10^{12} protons [30]. Thus, for the simulations a beam intensity of 3.08×10^{12} protons was chosen.

4.2 Sample analysis

After irradiation of the strands samples, several experiments were conducted to evaluate the damage in the samples left by the beam. This section will introduce those experiments which were used to validate the simulations. The experiments were mostly conducted batch by batch, so that most simulation results will be marked with a specific batch number. If this is not the case, the average for a given sample from multiple batches is shown.

4.2.1 Microscopic Inspection

Following the removal of the sample holders from the cryostat and the extraction of the strand samples, the samples were analysed for impact marks and other visual changes. Figure 4.3 shows example of microscope images of two strand samples. They show a clear deformation following the beam impact. Sample B2S8 (left) shows a characteristic kink in the impact position. On sample B2S9 (right) imprint marks of the sample holder are clearly visible.

From the visual inspection of the samples it was, thus, concluded, that the strands experienced important stresses from bending and or compression. Therefore, it is likely that these levels of deformation have an impact on the superconducting properties of the samples.

The inspection of the sample holder showed no evidence of local melting in the copper.

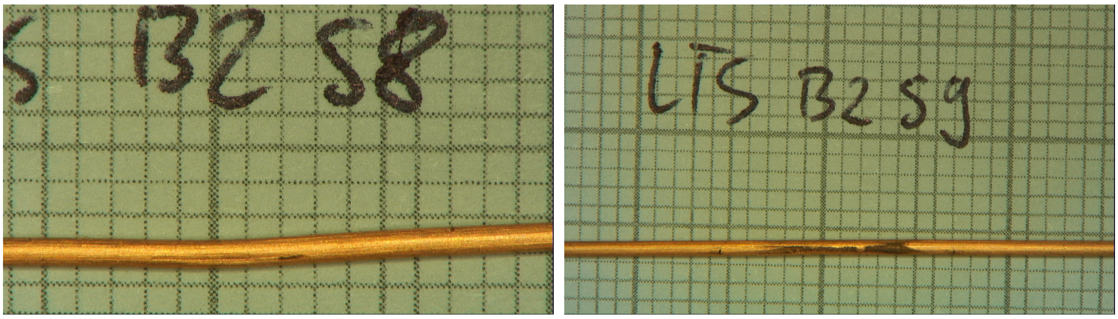

Figure 4.3: Examples of microscopic pictures of two strand samples, which clearly show a deformation following the beam impact. Sample B2S8 in the left picture is bent the beam impact position and sample B2S9 shows an imprint from the sample holder [30].

4.2.2 Microscopic Analysis of the Strand Cross Sections

To investigate the microscopic damage within the observable strands, they were cut into half cylinders to reveal the axial subfilament profile. Figure 4.4 shows the strand cross section which is investigated by the microscopic analysis in orange.

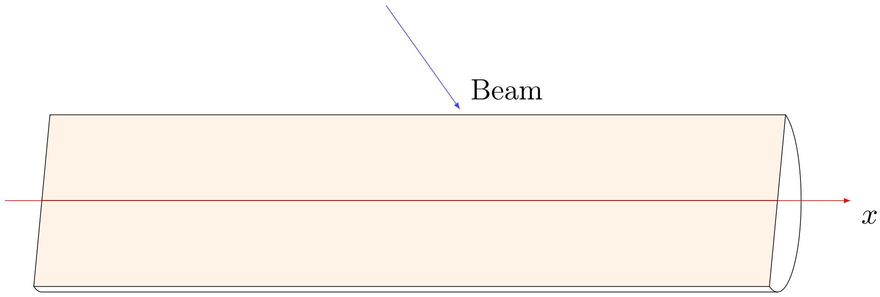

Figure 4.4: Schematic view of the ideal surface used for the microscopic analysis.

Ideally this cross section would be in the centre of the strand orthogonal to the beam axis z so that the gradient caused by the beam offset can be seen.[12]

Figure 4.5 compares two cross sections for a sample that experienced a small hotspot temperature(B1S1, top) and one where a larger hotspot temperature was reached (B1S6, bottom). The Nb_3Sn subfilaments are shown in grey and are surrounded by copper. On the bottom image, a large number of vertical hairline fractures are observable on the grey surface which are not observable on the top image.

Etching away the copper around the filaments, the exposed radial cracks were studied under a scanning electron microscope, some images of which are shown in Fig.4.6. The images reveal the difference between hairline fractures for lower hotspot temperatures (eg. S4, left) and bigger cracks for larger hotspot temperatures (eg. S6, right). The

[12]The samples are expected to have kinked in exactly this plane, which would cause them to lie on equi-z planes. Grinding them down in parallel to the ground, thus, reveals equi-z planes. Samples of lower hotspot temperature did not exhibit kinks. They are not necessarily presented in equi-z planes.

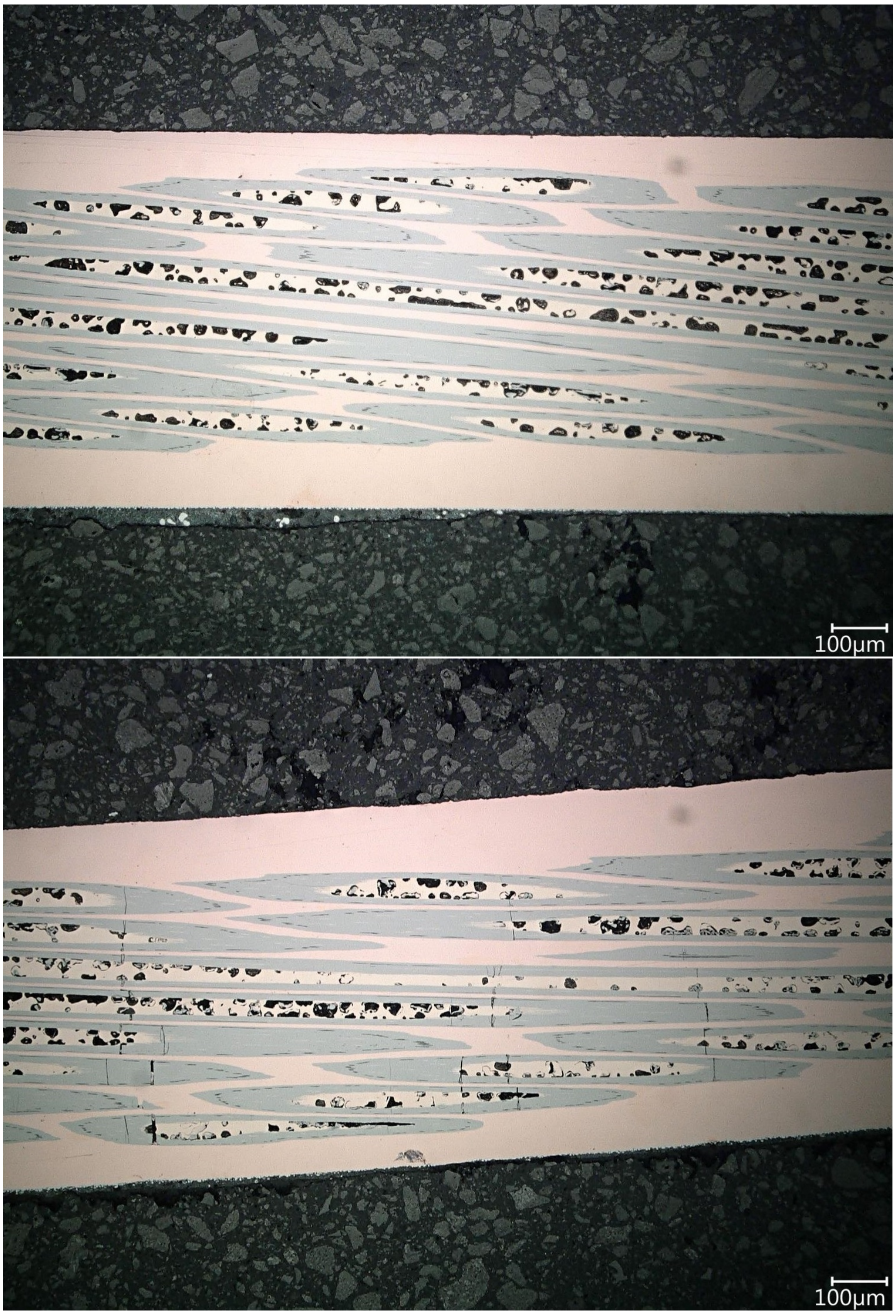

Figure 4.5: Optical x200 analysis of the ground cross sections of samples S1(top) and S6(bottom).
Courtesy of Mickael Meyer, EN-NME-MM, CERN

different scales on the two images have to be noted.

This inspection suggests:

- Radial cracks from S4 onwards
- More and bigger cracks with higher hotspot temperature

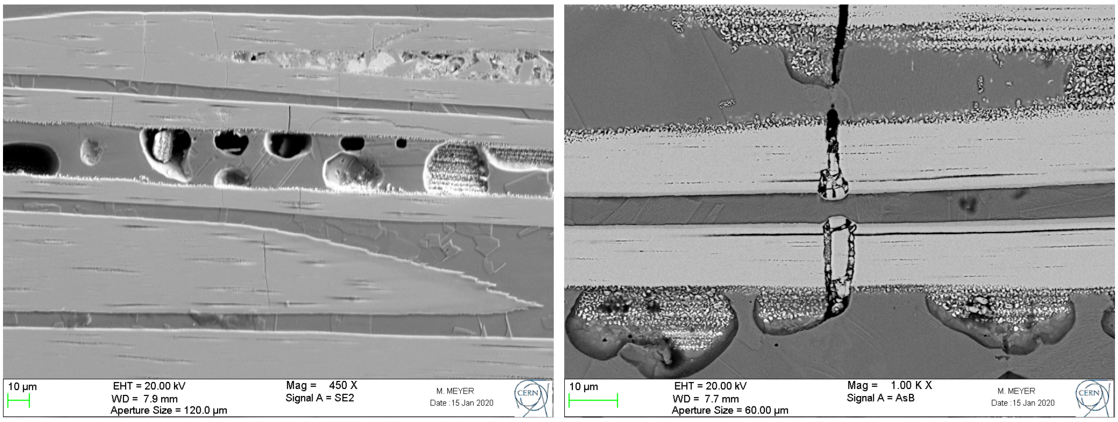

Figure 4.6: SEM analysis of the edged subfilaments of samples S4(left) and S6(right). Courtesy of Mickael Meyer, EN-NME-MM, CERN

4.2.3 Critical Current Measurement

Critical current I_c measurements of the impacted strands were performed at the Department of Quantum Matter Physics at the University of Geneva. During the measurements, the samples were exposed to magnetic fields with strengths in the range of 1...20 T, while held at a constant temperature of 4.2 K.

4.2.4 Magnetic Moment Measurement

To investigate the strain state distribution in the impact point of the samples a magnetic moment measurement was performed on a selection of samples. For this purpose $\sim$5 mm long pieces were cut out of the samples around the impact point. On these cut outs the magnetic moment was measured for a temperature sweep from 4 K up to 20 K at a constant external magnetic field of 1.2 mT. The change of magnetisation over temperature gives a measure of the critical temperatures T_c present in the strand.

5 Simulating the Beam Impact

The duration of the beam impact pulse of ∼600 ns is expected to be over quicker than classical thermo-mechanical effects in the target can take place. Furthermore, the deposited energy is too small to cause melting in the target. Thus, static parameters can be assumed regarding the beam impact and there is no need for coupling simulations. In this study, the following tools serve in a one way workflow pipe[13].

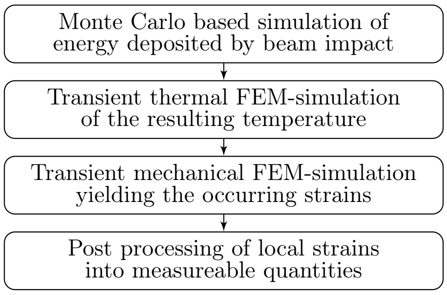

In this chapter, every step in this workflow will be explained in a dedicated section below.

5.1 Deposited Energy

In this study FLUKA was used to simulate the impact of a single incoming proton in the experimental set up. Figure 5.1 shows a cross section of the sample holder (copper colour) in which the samples (dark green) are placed. The strands were modelled as a single composite material, which fills the grooves of the sample holder. This material consists of copper and Nb_3Sn, where the fraction of Nb_3Sn was determined by the volume of non-copper materials in the strand. The radiation and scattering lengths are well above the characteristic lengths of the detailed strand geometry. Therefore, this approximation changes the calculated energy deposition only marginally in comparison to a more detailed strand model.

The generated probabilistic map of the proton's energy deposition is shown as a colour map in Fig.5.1. The energy deposition describes a cone shape which is typical for a hadronic shower (see 2.2). In the axial centre of the strands, the energy deposition grows with increasing penetration depth of the sample holder reaching a maximum of $\sim 10\,\mathrm{GeV\,cm^{-3}}$ per proton around $z = \sim -0.5\,\mathrm{cm}$ (sample S10). In all samples the deposited energy decreases very quickly along the axis of the strand underlining the localised nature of the expected damage.

For the readout stage of the simulation, Boolean detector volumes (in this case cuboids) are introduced that allow for mapping the energy deposition with cell-like binning. This 3D map of the energy deposition can consequently be interpolated and translated onto

[13] As part of the simulation pipe, the Monte Carlo simulations are described here. However it must be noted, that they were not conducted by the author.

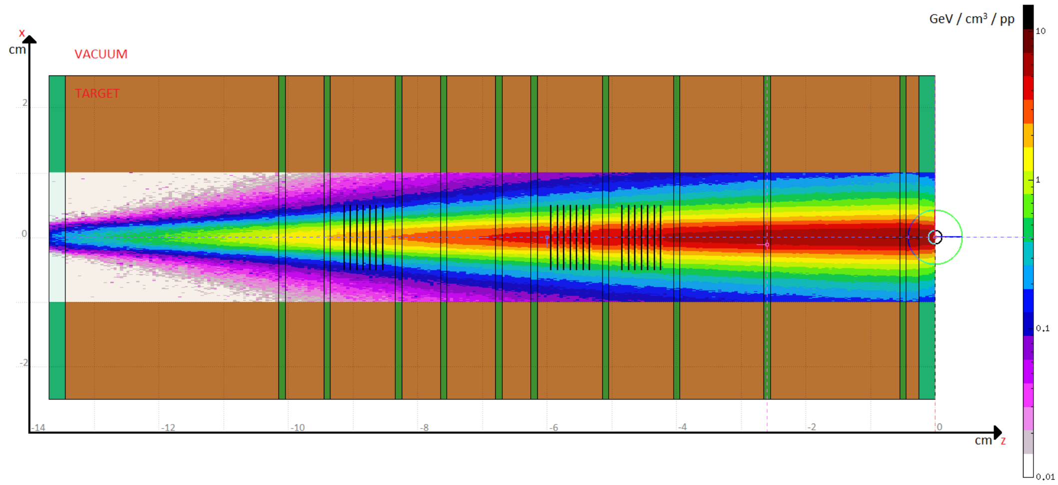

Figure 5.1: Energy deposition in $y = 0$ plane as calculated by FLUKA for one impacting primary particle. Copper colour represents copper, dark green represents the RRP strand material mixture, and light green represents stainless steel. The colour scale of the energy deposition is given in $\mathrm{GeV\,cm^{-3}}$ per primary proton.

geometries in other software. Multiplying the obtained energy deposition with the number of protons (beam intensity of $\sim 3.1 \times 10^{12}$) yields the expected energy deposition in the experiment. This can then be used as an input for the thermal simulation.

5.2 Thermal Profile

The next step of the workflow is to convert the generated static energy deposition into a time dependent temperature profile. Here the energy deposition is scaled into heating rates for a transient thermal simulation.

5.2.1 Simplifications for the Thermal Model

Transient simulations require a lot more computational effort than static simulations. This is further amplified by the use of non-linear material properties. The foremost goal of FEM model simplification is therefore to reduce the number of mesh nodes as far as possible. Since the beam hit the set up centrally with respect to the axial direction of the strands (x-axis), a symmetry plane in $x = 0$ is introduced. Furthermore only 30 mm above and below the strand groove of the holder geometry are considered in the model. The approximation is shown in Fig.A.5.

In the experiment the strands were surrounded by vacuum grease in the grooves to allow for thermal conductivity between the strands and the holder. This grease also served the purpose of holding the samples in place. However, the exact position of the strands in the grooves are unknown. In the simulations, they were assumed in the centre of the groove. The energy deposition map was generated with the Nb_3Sn strand filling out the groove. The actual density and atomic charge of the elements constituting the vacuum grease, however, are much lower than those of Copper or Nb_3Sn. Vastly overestimating the energy absorbed by the vacuum grease, this would result in overestimation of all temperatures. Trying to bypass this by not applying heating to the grease, on the other hand, would create a nonphysical heat sink. Therefore, the vacuum grease is omitted in the model and no thermal conductivity between samples and holder is allowed. This approach is further justified by the fact that even though the grease was introduced to allow heat flow from the samples to the holder, on short time scales it works as a thermal insulator.

In addition to the unknown location of the strands, also their orientation (no cylinder symmetry, see 2.3.2) during the impact is undetermined. In the simulations, the strands were simulated with a radially symmetric approximation. The area of the strand cross section in which the subfilaments lie is approximated with a circular band (from here on referred to as the matrix region). This region is assigned with the volume based average material properties of the constituent materials Nb_3Sn and copper. This model disregards other phases and materials present in the real strand (see 2.3.2). However, since Nb_3Sn and copper make up the vast majority of the strand, neglecting the contributions of other materials is justified. The remaining regions of core and jacket are modelled with high purity fully annealed copper with a RRR-value of 150 according to the strand's specifications.

5.2.2 Thermal Material Properties

To convert the heating into temperature T in the simulation, isobaric heat capacities C_p are used[14]. The temperature dependence of C_p for copper is well known [33, 34] whereas C_p of Nb_3Sn is only well documented from cryogenic temperatures up to 400 K [35]. Therefore, C_p of Nb_3Sn was extrapolated for higher temperatures.

A universal formulation for C_p is not readily available. Whence the Debye formulation of the isochroric heat capacity C_v

$$C_\mathrm{v} = 9 N k_\mathrm{B} x_\mathrm{D}^{-3} \int_0^{x_\mathrm{D}} \frac{x^4 e^x}{(e^x - 1)^2} dx \quad \text{where} \quad x_\mathrm{D} = \frac{T_\mathrm{D}}{T} \tag{5.1}$$

is used. Here, T is the temperature, T_D the Debye temperature of the material, N is the number of unit cells and k_B the Boltzmann constant. This is combined with a linear vibration dependence term to

$$C_\mathrm{p} = \alpha \cdot f_\mathrm{D}(T, T_\mathrm{D}) + \gamma \cdot T \quad , \text{where} \quad f_\mathrm{D}(T, T_\mathrm{D}) = x_\mathrm{D}^{-3} \int_0^{x_\mathrm{D}} \frac{x^4 e^x}{(e^x - 1)^2} dx \tag{5.2}$$

with α as a free fit parameter. The specific heat capacity coefficient $\gamma = 103\,\mathrm{mJ\,kg^{-1}\,K^{-2}}$ and $T_\mathrm{D} = 232\,\mathrm{K}$ are taken from literature [36, 37]. A least squares fit yields $\alpha = 721\,\mathrm{J\,kg^{-1}\,K^{-1}}$ and a function $C_\mathrm{p}(T)$ as shown in Fig.5.2.

[14] Isobaric heat capacities are chosen over isochoric formulations because they are more readily available in literature and the thermal solver doesn't consider changes in pressure or volume.

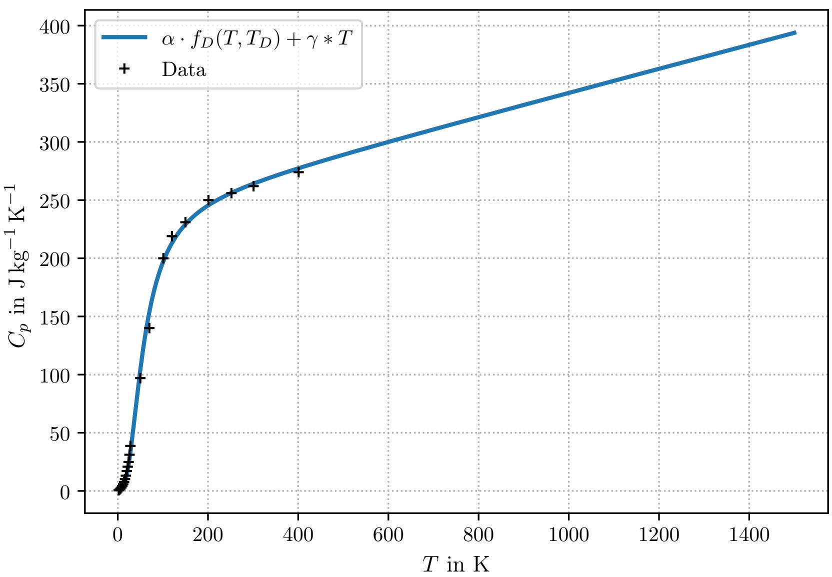

Figure 5.2: Heat capacity C_p of Nb_3Sn as a function of the temperature T. Equation (5.2) was fitted to the data points (black crosses) from [35].

The thermal conductivity of isolated Nb_3Sn above 300 K is still a topic of ongoing research. In the available range, the data indicates that it is significantly lower than that of copper (see Fig.A.4). Therefore the thermal conductivity of Nb_3Sn is set to zero for the generation of composite material properties. Furthermore, the model assumes isotropic thermal conductivity in the matrix region which is not given in the real strand due to the filamentary structure of the superconducting phase.

5.2.3 Transient Thermal Simulation

As a static code, FLUKA can not (by itself) generate a time dependent energy deposition required for a transient thermal analysis. As mentioned above, fundamental changes in the target occur only after the full duration of the beam. Therefore, the only constraint for a heating function is that for every node the time integral over the heating gives the respective energy deposition. Each shot consisted of 24 bunches with length of 0.3 ns and a spacing of 25 ns between bunches. To model this, binary step-functions can be imposed to the heating in the simulation. Because of the small bunch length, however, this leads to very large heating rates. For a continuous heating over the full impact length of 600 ns, the required heating rate is only ~1 % of that required for a pulsed heating. It is thus numerically more stable. The difference in the maximal temperature reached between a bunched heating with and a continuous heating over the whole impact time of 600 ns shows a maximal difference in the order of ~0.1 %. Therefore, the continuous heating method is chosen for its advantages in numerical stability.

This approach is implemented in the Transient Thermal analysis package of the commercial software ANSYS®.

In the experiment the entire set-up was cooled back to the base temperature after each shot. In the simulation, however, the holder and samples were simplified to being adiabatic. Therefore the equilibrium temperature in the simulated set up after the shot is above 4 K. However, it will be shown, that this does not influence the final result of the mechanical simulation.

5.3 Mechanical Response

Based on the generated time dependent temperature distribution, the mechanical response of the system can be studied. Following the above shown workflow, the next step is the use of a transient mechanical simulation package. Here the temperature based expansion and contraction interactions of the geometries were simulated.

5.3.1 Simplifications for the Mechanical Model

In thermal simulations, there are only few temperature dependent properties to consider. In mechanical simulations, in addition to the thermal dependencies there is, more importantly, also a nonlinear stress-strain dependence. Additionally, the use of quadratic elements doubles the node density for the same element resolution in comparison to the linear elements in the thermal simulation. This leads to a more complicated problem to solve. To keep the computation time reasonable, reducing the number of nodes is thus even more essential than for the thermal simulation.

For the mechanical simulation all of the simplifications discussed in 5.2.1 apply or were extended in the following ways:

Due to the vast rise in temperature, the grooves in the sample holder for samples at deeper beam penetration levels narrow to such an extend, that they touch the sample. Therefore, it is not possible to omit the sample holder completely.
A natural first idea would be to simulate only a single strand per simulation with only those slices of the sample holder in contact with the strand held by fixed surfaces on the far sides of the strand. Indeed, this speeds up the solution process significantly. Due to the short time scale of the impact however, the cumulative shock wave of the thermal expansion is the stronger the more of the expanding sample holder is taken into consideration. Therefore only modelling a few slices of the holder results in underestimating the forces exerted onto the samples by the sample holder. However, in the sample holder sets of metal foils were introduced at certain penetration depths along the beam axis to verify local maximum temperatures (see Technical Report [30]). Simulations showed, that these foils acted as a form of cushion for the shock wave propagation in the sample holder. This divides the sample holder along the beam axis into four separated impact zones (see Fig.A.5 and Fig.5.3).

Adding contact formulations adds to the run time of a mechanical simulation. This is especially true if the contact pair causes plastic deformations to one another as they do in case of the sample holder. Formulating the sample holder as a single body, rather than a set of individual slices with all sets of neighbouring slices representing a contact pair, makes the simulation a lot more stable and faster. However, the studies showed that it caused an overestimation of the shock wave propagation due to the lack of the limiting interaction surfaces of the individual slices. Therefore, it was important to introduce some contact surfaces dividing the body of the sample holder.

The final simulation model of the sample holder combines the above points. The model partitions the sample holder. Here, one partition reaches from one set of metal foils to the next. The approximation for the mechanical simulation is represented exemplary for sample S6 in Fig.5.3. The parts of the sample holder holding the foils are taken out as well, giving the same effect of stopping the shock wave propagation, but reducing the node count even further. These cutouts can be seen in Fig.5.3 (top) on both sides of the sample holder. On the far sides of those cutouts, fixed supports are implemented to imitate the interface with the rest of the holder. To account for the necessary contact surfaces in the regarded region, the two slices holding the sample are modelled as individual bodies with their original thicknesses. The resulting contact surfaces are marked in Fig.5.3 (top) in pink. The rest of the holder is modelled as two single bodies. The height of sample holder considered in the simulations was 60 cm. Like in the experiment, this guarantied the confinement of thermal expansion around the grooves in the vertical direction.

5.3.2 Contact Formulation and Meshing

The presence of the vacuum grease between sample and holder in the experiment makes it difficult to replicate the original contact in FEM. The symmetry of the problem in the $x = 0$ plane, however, suggests that there is little grinding of the surfaces, since the relative movement should (if at all) happen in the $x = 0$ plane. Thus, the interaction is likely dominated by the holder pressing into the strand and it is sufficient to assign a frictionless contact. Not including the vacuum grease as a buffer between two rigid surfaces could slightly overestimate the severity of the interaction between the two metal surfaces. A normal stiffness and restitution factor of 1 is, nonetheless, set as a best guess. The contact formulation between the sample holder parts is frictional and modelled as copper-copper contact with a friction coefficient of $\mu_\mathrm{f} = 1$ and a dynamic coefficient of $\mu_\mathrm{d} = 0.1$.[15]

The mechanical simulation required the use of quadratic mesh elements. The element size was adjusted such that the mesh density is high in the impact zone of the strands and low in parts of the sample holder far away from this zone. This allowed for a higher density in the region of interest without overshooting the overall node count. The mesh density could dynamically be adjusted by the program a maximum of two times.

[15]Detail for reproducibility: The penetration tolerance is set to 1×10^{-3} mm with a Nodal-Projected-Normal-From-Contact detection method.

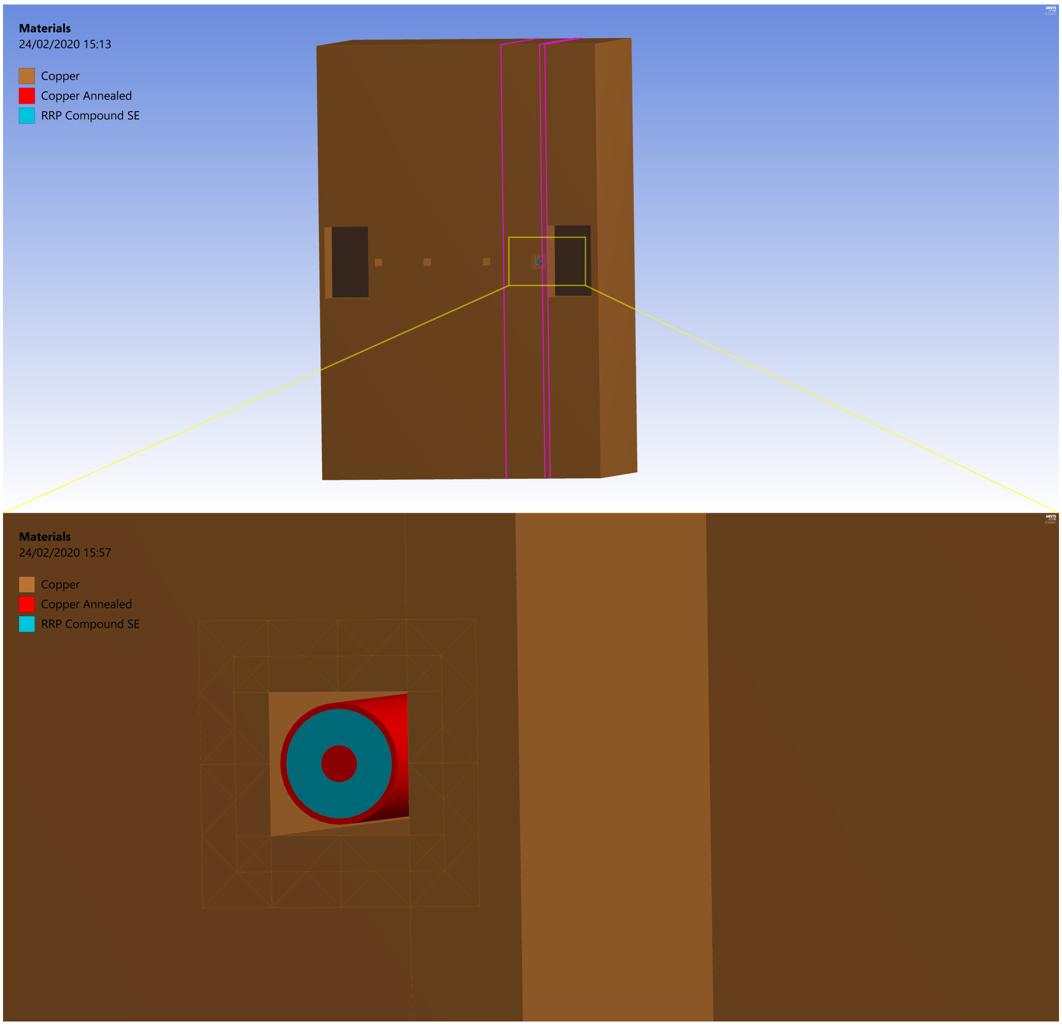

Figure 5.3: The geometry approximation used for the mechanical simulation shown in overview and close up exemplary for sample S6.
The strand is modelled from concentric cylinders, vacuum grease, temperature detecting metal foils and the in between ribs are neglected, sample holder layers outside of the immediate vicinity of the investigated sample are combined, samples other than the sample in question are omitted. 30 cm of the sample holder above and below the strand are included.
On the top image, the surfaces dividing bodies are marked in pink.
Cold cast copper is represented in copper colour, annealed copper in red, and the matrix region compound material in turquoise.
The markings on the sample holder around the groove (bottom) are added to guide the ANSYS® mesher to generate a locally symmetrical mesh.

5.3.3 Mechanical Material Properties

In the transient thermal simulations the temperature dependent variables used were only the thermal conductivity κ and the specific heat capacity C_p of the different materials. In the mechanical simulations these are the temperature dependent coefficient of thermal expansion α, the Young's modulus E, Poisson ratio ν and the speed of sound v_s. The system is, thus, inherently more complex and more susceptible to uncertainties in the material properties.

Nb_3Sn is a brittle material. This means that it reacts linearly to compression and tension up to its breaking point. Copper, bronze, tin and niobium, on the other hand are ductile materials, which undergo plastic deformation before they break. The simplification approach of homogenising the layer of copper matrix and subfilaments therefore involves assigning either of the properties. In case of plastic deformation of the ductile materials, an equilibrium between the Nb_3Sn tendency to return to its original state and the acquired deformation of the ductile materials would be reached. This can be justified, by tensile stress measurements performed on RRP® Nb_3Sn strands in [38], which resemble the behaviour of a ductile material.

Fully annealed copper is more ductile than the other materials present in the matrix area (bronze, tin, etc.). This means that the pseudo-plastic deformation of the strand stems from the matrix region. Therefore, for the simulation, the pseudo-ductile behaviour of the RRP® wire is assigned to the matrix region. The annealed copper parts in the model is assigned the ductile behaviour of fully annealed copper.

5.3.4 Transient Mechanical Simulation

The mechanical response of the system was simulated with the Transient Mechanical analysis package of ANSYS®.

The degradation of the superconductor is expected to be the most severe at the impact location. The critical current of a superconducting strand is given by its weakest cross section, which acts as a bottleneck for the supercurrent. Therefore, it is sufficient, to read out the parameters at the $x = 0$ symmetry plane to analyse the expected degradation.

As described in 2.3.2 an $I_c(\varepsilon)$ irreversibility cliff is well documented in literature, which can be explained as the superposition of plastic deformation and the tearing of filaments under strain. In the experiment the maximum total strain experienced by an individual subfilament of the strand is the likely cause of its cracking. For the analysis of this mechanism, the total strain maximum over time $\varepsilon_{\mathrm{tot,max}}$ (see 3.2.3), is read out for each node in the matrix region.

The microscopic theory predicts degradation of the superconducting properties of Nb_3Sn for lattice strain $\varepsilon_{\mathrm{lat}}$ in the superconducting phase. In the approximation of the model this is represented during the impact by the total strain $\boldsymbol{\varepsilon}_{\mathrm{tot}}$ of the matrix region. This would be relevant in describing the I_c of the strands during the beam impact. The simulation, however, is compared to the results of I_c measurements taken back at cryogenic temperatures. A part of the total strain during the impact is elastic and/or thermal. Thus, the relevant parameter for the comparison between experiment and simulation is the residual plastic strain $\boldsymbol{\varepsilon}_{\mathrm{pl}}$. Furthermore, this is also the case for a real magnet, which would be cooled after a potential impact, thus only being affected by residual damage.

Figure A.8 shows the final output of the simulation post processing as a function of the set simulation end time. It shows that above a simulation length of 30 µs the final result does not change anymore. Therefore, the simulation length is set to 100 µs, to leave a sufficient error margin on the analysis.

5.4 Simulation Post Processing

To make a quantitative statement about the simulation accuracy, the mechanical output of ANSYS® had to be converted into observable parameters of the strands. These parameters are the critical current I_c, the upper critical magnetic flux density B_{c2} and the critical temperature T_c. The basic assumption of this interpretation is that the strain state of the single strands is equivalent to that of the average matrix region in the model. For example, the residual plastic strain ε_{pl} of a given node of the matrix region is interpreted as equivalent to the lattice strain state ε_{lat} of the local Nb_3Sn phase after cool down. This is assumption is justified in this context, as the empirical data for the scaling laws and material properties used relies on single strand measurements. The analysis will mostly focus on the axial strand cross section that is closest to the beam impact ($x = 0$).

5.4.1 Mentink-Arbelaez-Goedeke Scaling

To derive the strands overall I_c, the critical current density J_c has to be calculated first. The workflow implemented to calculate J_c is shown in Fig.5.4. Here, the residual first principal strain ε_1 is taken from the thermo-mechanical simulations in ANSYS® as an input. Based on the MAG scaling (Eqn.(2.13)) this strain is used to calculate the degradation of T_c, B_c and finally J_c[16] according to Eqn.s (2.12), (2.11) and (2.10).

Due to the large temperature gradients caused by the beam, and the sample holder influence on some parts of the strand, the strain distribution over the cross section is highly non-uniform. This then leads to a similarly non-uniform J_c-distribution. If such a strand is operated at its overall I_c, the current will be shared unevenly between the subfilaments, depending on their maximum capacity.

5.4.2 Filament Cracking Model

The histogram count of cracked filaments mentioned in 2.3.2, and shown in Fig.A.1 has the shape of a slightly modified probability density function Maxwell-Boltzmann distribution:

$$pdf_{\mathrm{MB}}(x,\sigma) = \sqrt{\frac{2}{\pi}}\frac{x\exp\{-(x/\sqrt{2}a)^2\}}{a^3} \tag{5.3}$$

[16] Conventionally J_c is defined by the superconducting current divided by the surface area of all non-copper (non-Cu) materials.

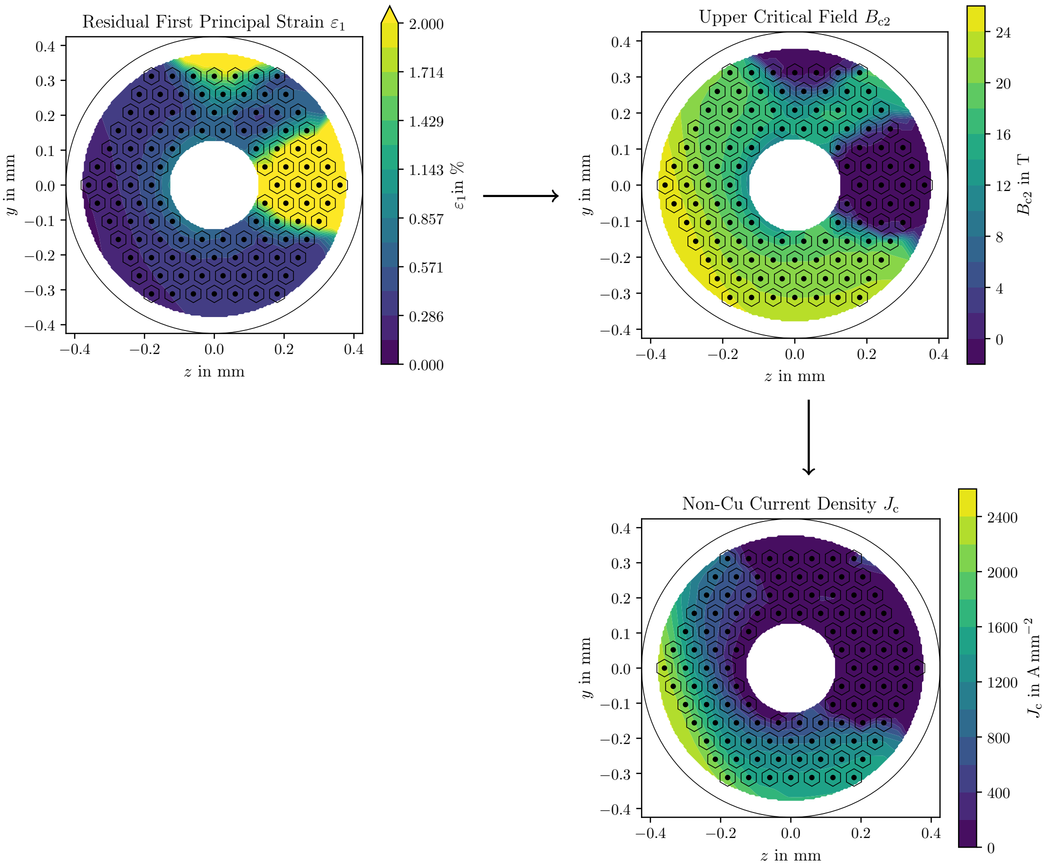

Figure 5.4: Calculation workflow based on MAG strain scaling and (2.10). Sample 7 is shown as an example. The values were calculated for a temperature $T = 4.2\,\mathrm{K}$ an applied magnetic field $B_{\mathrm{app}} = 12\,\mathrm{T}$. The hexagons indicate the position of the superconductor in the real strand in an arbitrarily chosen orientation.

The pdf_{MB} is remodelled into the desired form under the transformation

$$x = \varepsilon_{\mathrm{irr}} + 4\sigma - \varepsilon_{\mathrm{tot}} \tag{5.4}$$

This function is interpreted as the actual *pdf* to find a filament cracked, based on its strain state. This implies the definition of the irreversibility cliff $\varepsilon_{\mathrm{irr}}$ as the total strain $\varepsilon_{\mathrm{tot}}$ at which none of the filaments are broken with a 2-σ certainty.

The cumulative distribution function of the Maxwell Boltzmann distribution is given by

$$cdf_{\mathrm{MB}}(x, \sigma) = erf\left(\frac{x}{\sqrt{2}a}\right) - \sqrt{\frac{2}{\pi}}\frac{x\exp\{-(x/\sqrt{2}a)^2\}}{a} \tag{5.5}$$

where erf is the error function. The $cdf_{\mathrm{MB}}(x)$ under transformation (5.4) of a given $\varepsilon_{\mathrm{tot}}$ can be used as a statistic filament cracking weight w for the degradation of J_{c}. Figure 5.5 shows the distribution of cracks in the filaments of a strand in case of a uniform axial strain $\varepsilon_{\mathrm{ax}}$ (top) and the corresponding applied weight function (bottom).

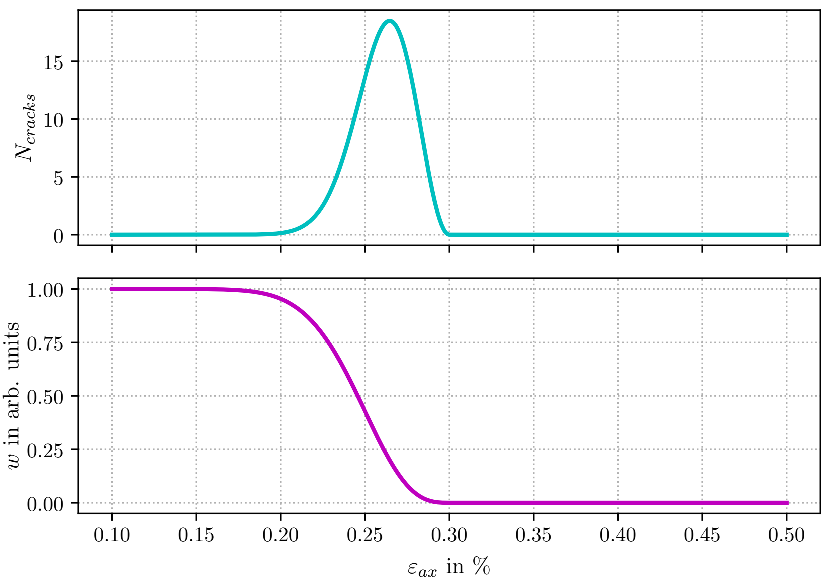

Figure 5.5: Expected crack distribution for a wire with 127 sub filaments and its according scaling function. The graphs are calculated for: $\varepsilon_{\text{irr},0} = 0.2\%$, $\sigma_{\text{cliff}} = 0.05\%$. These values serve for illustration and were not used in the studies.

A crack of a filament should only affect the current the filament can carry. Thus, w is only applied to the final J_c calculated from ε_{lat} rather than applying it to ε_{lat} directly.[17]

This idea is used to extend the workflow shown in Fig.5.4. If a filament cracks or not will be determined by the maximum overall strain that it experiences as a result of the beam impact. Therefore, the maximum total strain $\varepsilon_{\text{to,max}}$ in the $x = 0$ is taken from the thermo-mechanical simulations. This is used as an input for the cracking weight factor w determined by Eqn.(5.5) under the transformation described in Eqn.(5.4). In this study, ε_{irr} and σ_{cliff} used in Eqn.s(5.5) and (5.4) result from a fit (this fit will be explained in 5.4.4)[18]. The resulting workflow is shown in Fig.5.6.

5.4.3 Self Field Correction

The superconducting currents in the sub filaments generate magnetic fields. Due to the symmetry of the wire substructure, the magnetic field vectors cancel each other out in the centre of the strand. Thus, the self field strength grows from 0 in the centre to a maximum value on the surface of the conductor as shown in Fig.A.6. In the case of asymmetrical current distribution as is present in the experimental strand samples,

[17]Because fracture is connected to strain release, T_c and B_{c2} are actually expected to increase. Modelling this however is difficult, as the surrounding ductile materials will still keep the Nb_3Sn under strain. This would require knowledge of the strain states of the separate phases. These, however, were not modelled in the simulation.

[18]If future experiments can quantify the cracking of Nb_3Sn subfilaments more thoroughly, these values can adopted to the experimental findings.

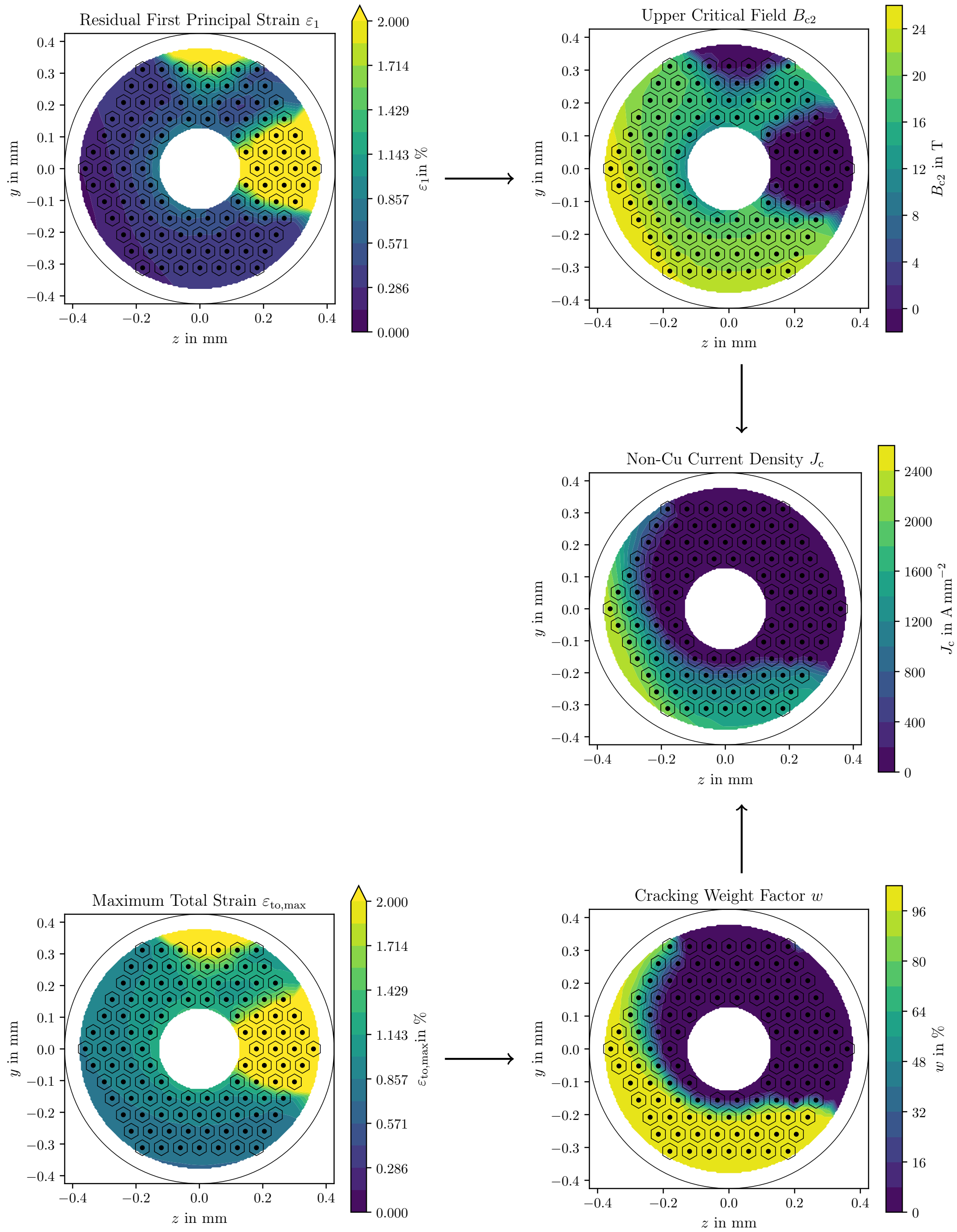

Figure 5.6: Calculation workflow based on MAG strain scaling, Eqn.2.10, and additional cracking weight w. Sample 7 is shown as an example. The values were calculated for a temperature $T = 4.2\,\mathrm{K}$ an applied magnetic field $B_{\mathrm{app}} = 12\,\mathrm{T}$. The hexagons indicate the position of the superconductor in the real strand in an arbitrarily chosen orientation.

however, the resulting magnetic field strength distribution will also be asymmetrical.

All nodes are now assumed to be conductors that are point-like in the $y - z$ plane and infinitely long along x. The magnetic field generated by one node can be calculated using the law of Biot-Savart

$$\vec{B}(\vec{r}) = \frac{\mu_0 I}{2\pi r}\vec{e_\phi}. \tag{5.6}$$

Here, μ_0 is the vacuum permeability, r the distance of the conductor and $\vec{e_\phi}$ is the unit vector perpendicular to the radial direction in polar coordinates of the plane. The magnetic field that node n' sees is calculated as the sum over the magnetic field vectors induced by all nodes $n \neq n'$ in the discretised form

$$\vec{B}_{\mathrm{n'}}(\vec{r}) = \frac{\mu_0}{2\pi}\sum_{\mathrm{n}\neq\mathrm{n'}} I_{\mathrm{c,n}}\vec{e_{\mathrm{x}}} \times \frac{\vec{r_{\mathrm{n}}} - \vec{r_{\mathrm{n'}}}}{\|\vec{r_{\mathrm{n}}} - \vec{r_{\mathrm{n'}}}\|^2} \quad , \tag{5.7}$$

where $I_{\mathrm{c,n}}$ refers to the nodal critical current I_{c}, and $\vec{r_{\mathrm{n}}}$ denotes the nodal coordinate vector in the $y-z$ plane. This discretisation is only justified for an equally spaced mesh of the cross section, but can be generalised by applying a weight function to the nodes depending on the area they represent. The orientation of the sample with respect to the applied magnetic field during the I_{c} measurements is not known. The external magnetic field will here be assumed parallel to the self field, yielding the scalar correction term $B_{\mathrm{n}} = \left\|\vec{B_{\mathrm{n}}}\right\|$.

Applying this formulation to every node yields the self field distribution shown in Fig.5.7 for the simulation results of sample S7 at I_{c} for an applied magnetic field $B_{\mathrm{app}} = 12\,\mathrm{T}$.

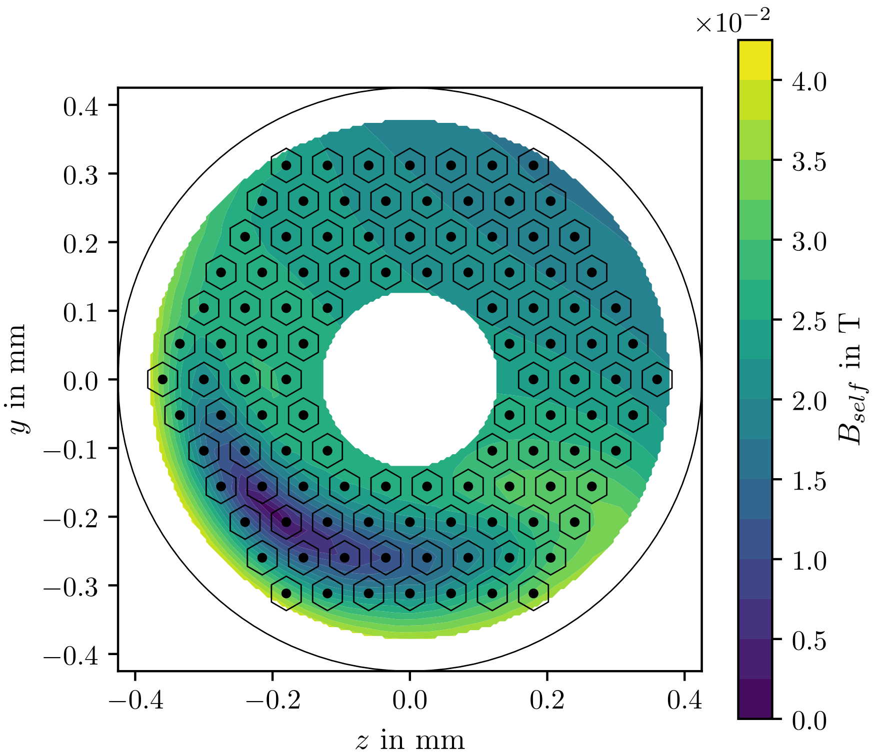

Figure 5.7: Self field of sample S7 at I_{c}. This map is calculated for the strand at I_{c} from the simulated strains for $T = 4.2\,\mathrm{K}$ and an external magnetic field $B_{\mathrm{app}} = 12\,\mathrm{T}$

For larger applied magnetic fieds B_{app} the critical current densities J_{c} are lower, leading to a smaller self field. As Fig.5.7 shows, the self field influence at I_{c} for larger magnetic fields can be very insignificant (here in the order of 0.1 %). For smaller magnetic fields, however, the current densities are much higher, and thus the resulting self field needs to be taken into account.

5.4.4 Critical Current Integration

The surface integration of the J_{c}-distribution is approximated by a sum over the J_{c}-values calculated for each mesh-node. The I_{c} formulation

$$I_{\text{c,strand}} = \iint_{A_{\text{CS}}} \vec{J}_{\text{c}}(\vec{r}, B_{\text{app}}, T, \varepsilon_{\text{lat}}) d\vec{A} \tag{5.8}$$

can be discretised as

$$I_{\text{c,strand}} = \alpha \cdot \sum_{N_{\text{nodes}}} J_{\text{c,n}}(B_{\text{app}}, T, \varepsilon_{\text{lat,n}}) \tag{5.9}$$

where B_{app} is the applied magnetic field, T is the temperature and α is a normalisation constant.

To determine α the theoretical ($\varepsilon_{\text{lat}} = 0$, $T = 4.2\,\text{K}$) curve is scaled to the highest measured I_{c} of the reference sample for a single external B-field. Because the scaling is done for only one field value, it doesn't affect shape of the $I_{\text{c}}(B_{\text{app}})$ curve. Moreover, the same scaling is applied for all samples. Thus, it has no influence on the relative degradation between the samples.

Taking into account the self field correction, Eqn.5.9 becomes

$$I_{\text{c,strand}} = \alpha \cdot \sum_{N_{\text{nodes}}} J_{\text{c,n}}(B_{\text{app}} + B_{\text{n}}, T, \varepsilon_{\text{lat,n}}) \quad , \tag{5.10}$$

where B_{n} is the self field corrected magnetic field at node n. Since the self field correction results in a new J_{c} distribution, which in turn leads to a different self field correction. This can be solved numerically, by implementing implementing a do-while loop. The loop iterates the problem until the change in the overall I_{c} for a consecutive iteration step falls under a given threshold.

As described in Fig.5.6, filament cracking influences J_{c} and thus needs to be taken into account for I_{c} integration. Literature [23] shows how this cracking varies for different Nb_3Sn wire types. Thus, it is hard to accurately quantify the cracking parameters. In order to derive the input values required for the model described in 5.4.2 - ε_{irr} and σ_{cliff}- simulated I_{c}-curves were fitted to the measurement data using a least square fitting algorithm. This fit could be used on every single sample, given the fact that the ultimate strength of materials is temperature dependent. The resulting $I_{\text{c}} - B_{\text{app}}$ fit results are shown in Fig.6.6 and will be discussed in 6.2.

5.4.5 Upper Critical Field Analysis

The upper critical field B_{c2} is another parameter, which can be compared between measurements and simulation. Measuring B_{c2} at 4.2 K(boiling temperature of helium) would require magnetic fields in the order of ∼27 T. However, B_{c2} can be derived from linear extrapolation of the $I_c(B_{app})$ data in the Kramer form. It can be shown, that the extrapolation of the Kramer fit of a superposition of strain states will always yield a lower B_{c2} value than the maximum of individual strands. Thus, the best comparable value is derived from also fitting the simulated I_cs in the Kramer form for the same applied magnetic fields.

5.4.6 Critical Temperature Analysis

The measurement of the Magnetisation M for different T in a very weak magnetic field (as shown in 4.2.4) is equivalent to measuring how much of the superconducting material is still able to carry a shielding current. Since the magnetic field is weak, all parts of the superconductor that are below their local T_c will be able to do this. Parts that are above it however, will not. In the simulation this can be approximated by the number of cells of the same volume, which are still below their T_c at a temperature T. The derivative of $\frac{\mathrm{d}M}{\mathrm{d}T}$, thus, gives a T_c-density-distribution ϱ_{T_c} of the strand.

The magnetisation M was measured for a volume around the $x = 0$ cross section close to the beam impact. Therefore, a similar volume of the simulated strand has to be used for the comparison with the measurement results. To ensure cells with the same volume in the simulation, the nodal values of ε_{lat} in the matrix region are interpolated to a regular cuboid mesh. Each cell has, a distinct T_c by Eqn.s (2.13) and (2.12). A histogram count of these cells gives a T_c-density distribution much like the one that was derived from the $M(T)$ measurements.

In real superconductors, T_c varies locally as function of the tin content [39]. This leads to a spread around $T_{c,0}$ in the data derived from the $M(T)$ measurements for non-degraded samples. This variation was approximated in the simulations by applying a Gaussian filter on the histogram-counts. This analysis allows a relative comparison of the T_c-density distributions of different samples and of simulation results with measurement results.

The resulting T_c-density distribution curves are shown in Fig.6.1, where the areas below the curves are normalised to 1. This normalisation is required to allow the comparison to the measured magnetisation.

6 Simulation Results

The hotspot temperatures given in this thesis are derived for a beam impact with the same beam parameters, on a solid block of copper instead of the sample holder. This underestimates the temperatures reached in the samples by up to 40 % when compared to the thermal simulations. From the point of machine protection, however, this gives a conservative estimate of when to expect which kind of damage. Furthermore, such a value can be quickly simulated for an estimate in case of beam impact in the machine. The reference to samples on the other hand, will refer to the exact conditions in the experiment associated with respect to the position in the sample holder and the beam.

In this chapter, the methods presented in 5.4 are applied on the data obtained from simulations as described in 5.3. The simulations for samples S8(890 K) and higher did not converge when the sample holder was considered. Therefore only samples S1 to S7 are presented here.

6.1 Residual Strain Model

Figure 6.1 shows the simulated critical temperature density curves. Comparable to a real experiment, the T_c values have been derived for a central volume around the beam impact point. All simulated cutout volumes have the same length. The presented data is based on an assumed $T_{c,0}$ of 17.1 K. In addition, a Gaussian filter was applied to the data, as explained in 5.4.6.

With increasing hotspot temperature, the ϱ_{T_c} curves widen and tails towards lower T values become more pronounced. This results in a continuous decrease in the curve amplitude due to the enforced normalisation of the curves. Additionally, the point of the curve maximum is shifted towards lower T with increasing hotspot temperature. For sample S2 (350 K) no change of the ϱ_{T_c} curve is observable with respect to S1.

As discussed in 5.4, the critical current I_c of a strand is determined by the supercurrent bottle neck along the strand. In this case it is the cross section closest to the beam ($x = 0$). The first principle residual strains in these cross sections were converted into J_cs according to the workflow presented in Fig.5.4. Applying Eqn.(5.9) for the different samples yields the critical current as a function of the applied magnetic field ($I_c(B_{app})$) shown in Fig.6.2. With hotspot temperature there is a degradation in I_c over the entire magnetic field range. This degradation sets on noticeably with S4, while samples S1 to S3 exhibit little to no reduction in I_c. Among the more strongly degraded samples, sample S5 (640 K) is an outlier, showing larger reduction in I_c than even sample S7 (800 K). This can be explained by S5's unique position in the sample holder, causing a stronger sample holder influence.

The I_c data can be represented in the Kramer form (Eqn.(2.9)) which is shown in Fig.6.3, where the relative differences discussed above are also observable. The highlighted points represent the applied magnetic field strengths for which I_c was measured in the experiment. These data points are then used for as sampling points for a linear least squares

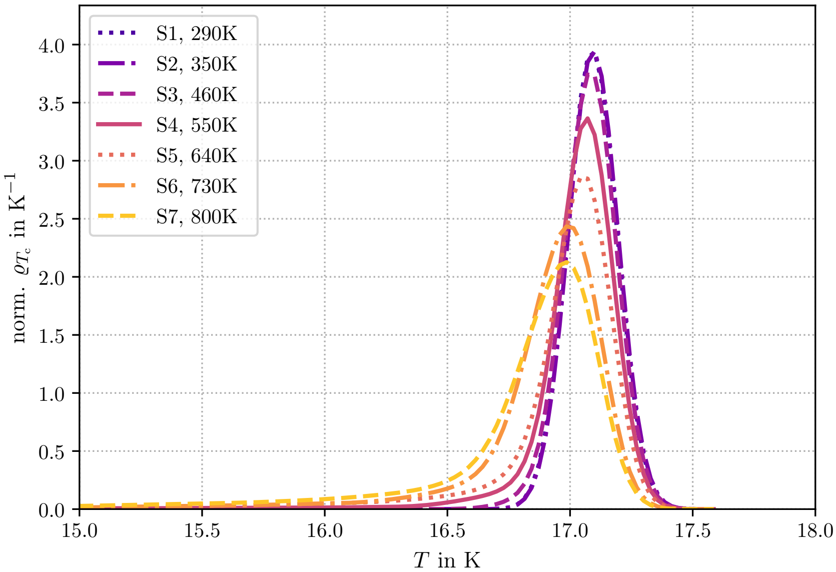

Figure 6.1: Critical temperature density ϱ_{T_c} profiles as a function of Temperature T. The data is simulated with sample cutouts of normalised length 4.5 mm around the beam impact centre. A Gaussian filter with σ=150 mK is applied.

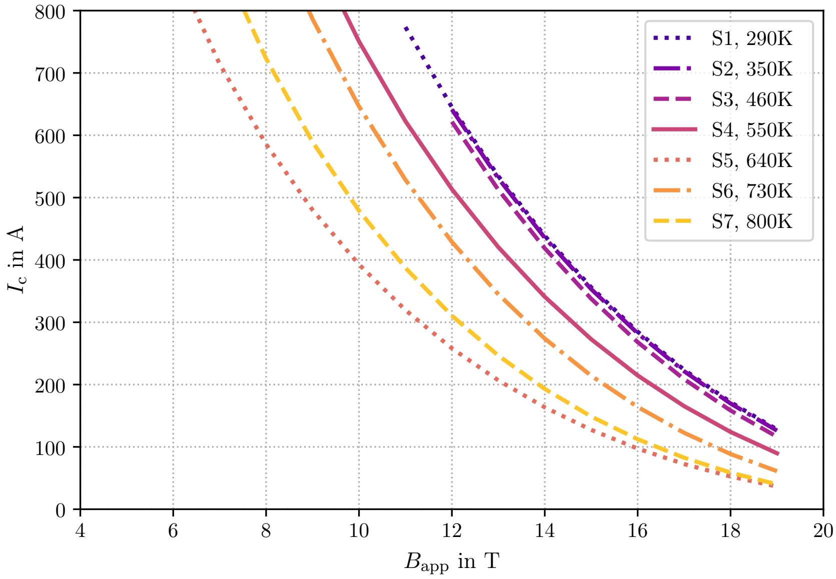

Figure 6.2: Critical current I_c as a function of the applied magnetic field B_{app}. The values are derived from the first principle strains in the central cross section.

fit (represented grey). As an effect of the superposition of different strain states, the simulated points do not align perfectly with the linear fit, but describe a slightly concave shape. The severity of the concave effect is a measure of strain gradients in the cross section. The effect is most prominent for samples S6 and S7.

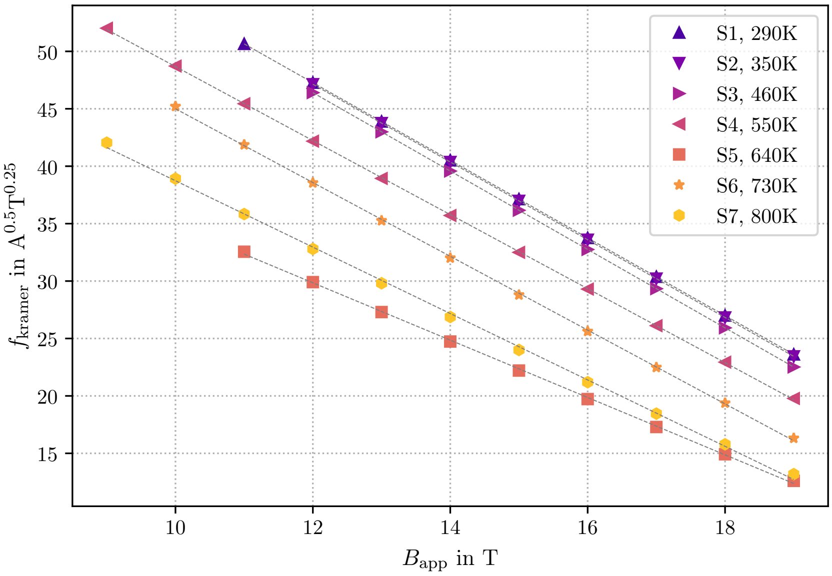

Figure 6.3: Critical current I_c as a function of the applied magnetic field B_{app} represented in the Kramer form. The values are derived from the first principle strains in the central cross section. The grey lines indicate linear fits of the shown data points.

The evaluation of the x-axis intersection for the linear fits in 2.9 yields a strand bulk B_{c2} and is represented in Fig.6.4. With increasing hotspot temperature (sample number), B_{c2} decreases. Again sample S5 (640 K) breaks the observed monotonous hotspot temperature dependence. This suggests, that in addition to the complete destruction of parts of the strand, the sample holder interaction also results in residual strain in other parts of the matrix region.

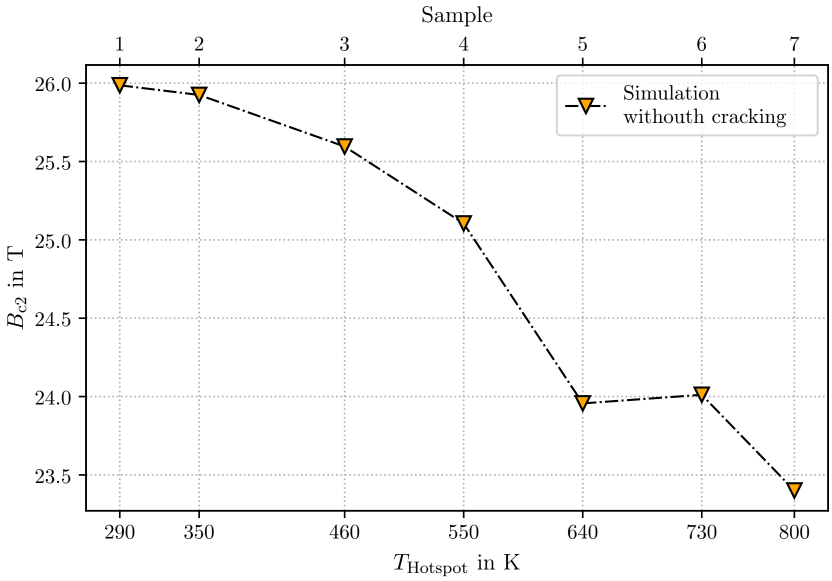

Figure 6.4: Bulk second critical magnetic field strength B_{c2} for the simulated samples. The values are derived from linear fits on simulated I_c values in the Kramer form (shown in Fig.6.3). Linear interpolations between data points were included for better comparability.

6.2 Filament Cracking Model

To describe the onset of filament cracking it is important to show, that the derived formulation does not change the results for the samples in which no filament cracking is expected. Figure 6.5 shows samples S1, S2, S3, and S4 evaluated with the same filament cracking analysis. Sample 4 exhibits degradation beyond that due to the residual strain (see Fig.6.2). The samples of lower hotspot temperature remain barely degraded. The J_c values used to calculate $I_c(B_{\mathrm{app}})$ (see 5.4.4) were calculated using the workflow shown in Fig.5.6 with the parameters shown in Tab.6.1.

Table 6.1: Fit of data to measurements using the cracking model described in 5.4.2 for sets of samples

Sample	$\varepsilon_{\mathrm{irr},0}$ in %	σ_{cliff} in %
S1, S2, S3, S4	0.5685	7.748×10^{-6}

An individual cracking analysis fit was done for every simulated sample. The fit result parameters are given in Tab.6.2. Figure 6.6 shows the calculated I_cs as a function of the applied magnetic field B_{app}. Qualitatively, the plot is similar to Fig.6.2, where samples S1, S2 and S3 show little to no degradation, and from S4 onward, the degradation is clearly observable. The severity of this degradation however is amplified by the cracking mechanism. Furthermore, the order of samples S5, S6 and S7 with respect to their degradation is reversed, such that now the degradation increases with hotspot temperature. The outlier here is S6, which was impacted by the sample holder in a way that the damage does not align with the expected cracking. The data was calculated using the

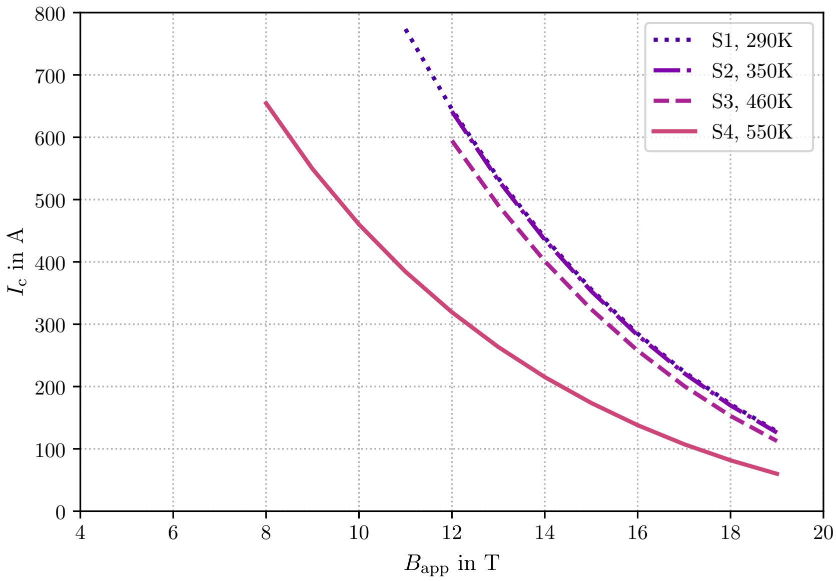

Figure 6.5: Critical current I_c as a function of the applied magnetic field B_{app}. The I_c values are derived as shown in Fig.5.6. The used parameters were fitted for the set of samples S1 to S4 and are shown in Tab.6.1).

workflow shown in Fig.5.6 with the parameters shown in Tab.6.2.

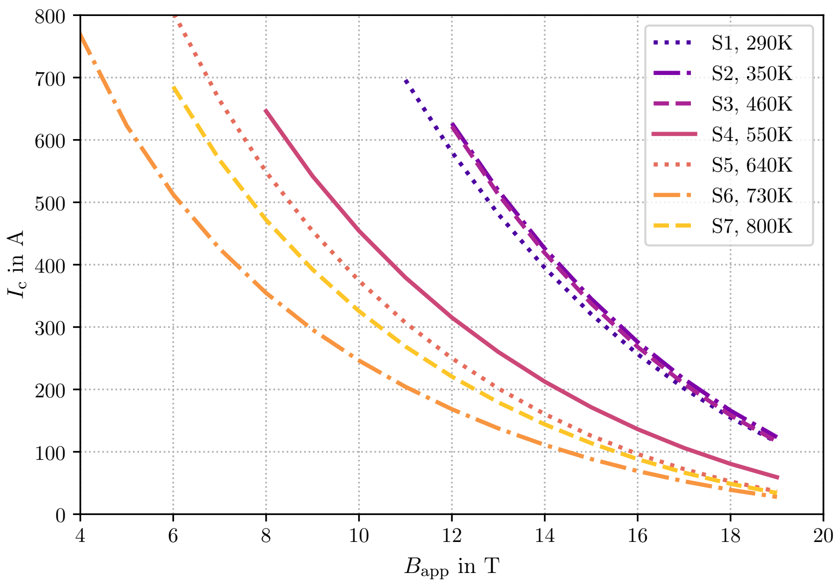

Figure 6.6: The calculated critical current I_c as a function of the applied magnetic field B_{app}. The critical current is calculated for different samples from both the residual strain and the the cracking influence in the central cross section as described in 5.4. The calculations rely on individual sample fits with the parameters represented in Tab.6.2.

Again, the data shown in Fig.6.6, can be represented in the Kramer form. This is shown

Table 6.2: Fit results for the cracking model described in 5.4.2 for each sample. The data is visually represented in Fig.A.7.

Sample	$\varepsilon_{\mathrm{irr},0}$ in %	σ_{cliff} in %
1	0.2797	1.367×10^{-4}
2	0.3967	1.490×10^{-5}
3	0.7056	2.361×10^{-3}
4	0.5548	7.318×10^{-3}
5	1.074	1.242×10^{-4}
6	0.778	2.777×10^{-3}
7	0.9099	3.379×10^{-2}

in Fig.6.7. In this plot, the calculated data points align better with the linear fits than in Fig.6.3. This is because cracking is expected for high strains. Because the large strain contributions no longer participate to I_c, the possible gradients are smaller, resulting in an effectively more homogeneously strained cross section.

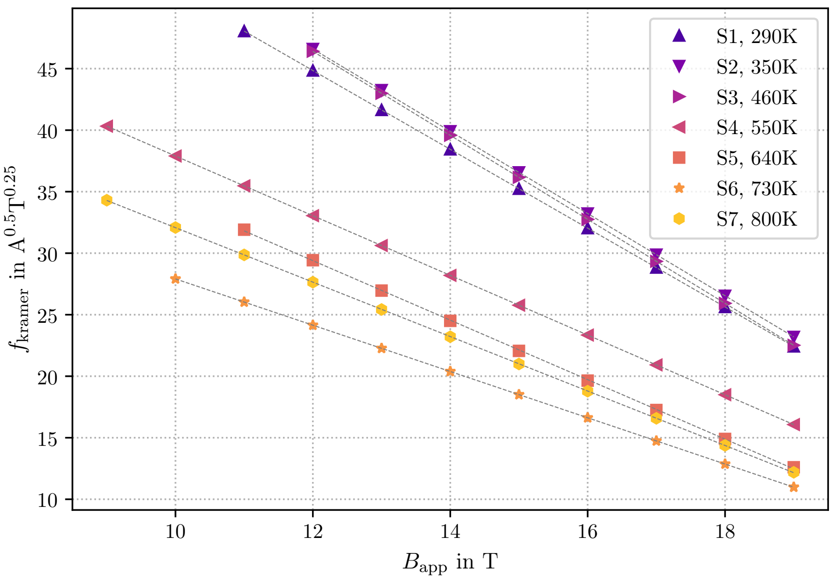

Figure 6.7: The calculated critical current I_c as a function of the applied magnetic field B_{app} in Kramer form. The criticial current is calculated for different samples from both the residual strain and the the cracking influence in the central cross section as described in 5.4. The calculations rely on individual sample fits with the parameters represented in Tab.6.2.

The extrapolated x-axis intersection of the linear fits shown in Fig.6.7 yields a bulk B_{c2} for each sample. This is shown in Fig.6.8. In comparison to Fig.6.4, the extrapolated B_{c2} is shifted towards higher values. For sample S4, the expected degradation due to filament cracking makes a significant difference in the absolute I_c values. The resulting extraplotion leads to a very strong rise in B_{c2}, even surpassing that of S3. For sample S5, the rise of B_{c2} is not as strong as for the other samples, wherefore it again breaks the monotonous hotspot temperature dependence.

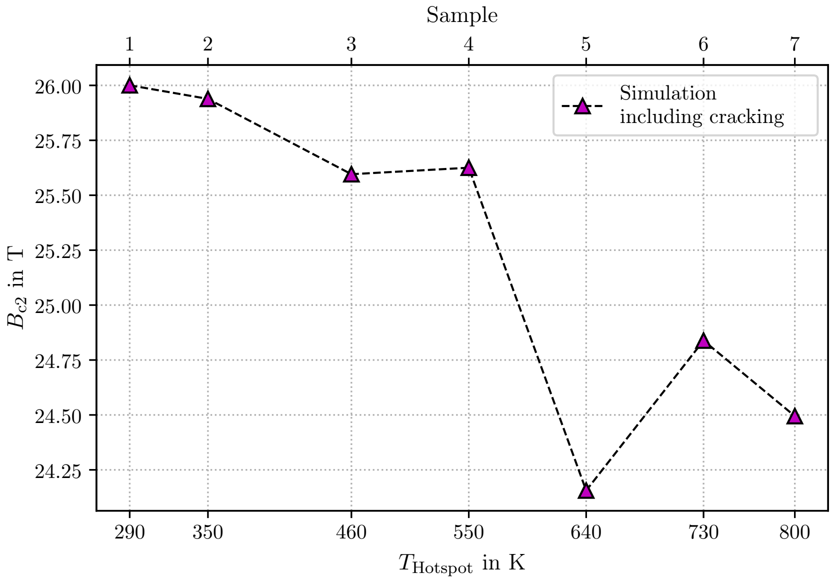

Figure 6.8: Upper critical field B_{c2} values extrapolated from linear fits in the Kramer form (Fig.6.7) for the simulated samples. The data considers strain dependence as well as filament cracking (shown in Fig.6.6). Linear interpolations between data points were included for better comparability.

6.3 Results for Free Samples

The sample holder has a significant influence on the degradations of the samples. It is, thus, also important to look at the expected results of I_c degradation, when only the beam heating of the samples is considered as a damage source. Because there is no data to compare this method to, only the degradation due to residual strain will be taken into consideration.

The resulting $I_c(B_{app})$ curves for the simulated samples are shown in Fig.6.9. The onset of expected degradation is by far less prominent in comparison to when the sample holder is respected. Due to the lack of sample holder influence, there is a monotonous dependence of the degradation to hotspot temperature.

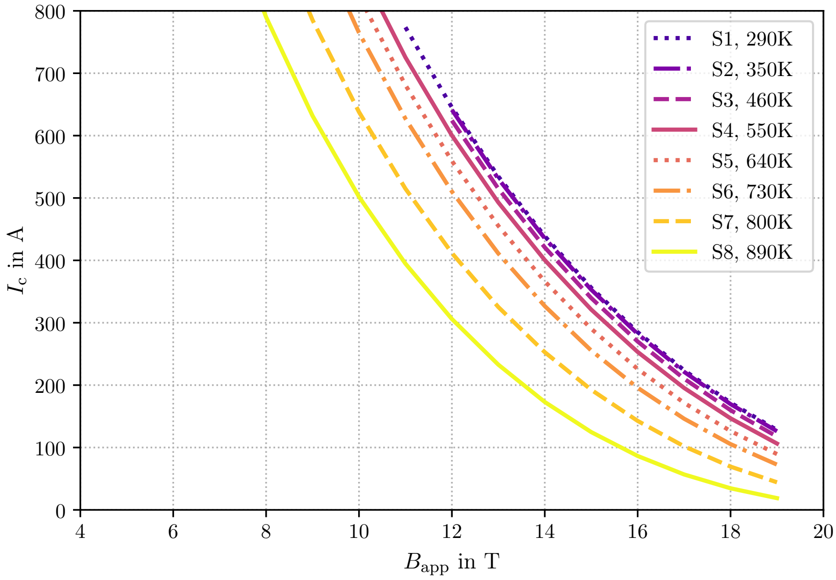

Figure 6.9: The critical current I_c as a function of the applied magnetic field B_{app}. The data was calculated for residual first principle strain. The samples were simulated disregarding the mechanical effects of the sample holder.

7 Simulation Error Estimation

Due to the complexity of the presented simulation workflow it is not reasonable to calculate the propagation of possible errors. This section will, therefore, only give an overview of different effects impacting on the final result, which is the critical current of a strand $I_c(B_{app})$ relative to that an undegraded strand $I_{c,0}$. The errors are divided into two groups. The first consists of such, where a sensitivity analysis of input parameters can give a ΔI_c. The uncertainties in the second group can not be quantified as a variable input parameter for an error propagation simulation. For this second group only an error estimate can be given. This thesis is, only going to focus on an error estimation for the simulations. For an error estimation of the experiment please find [32].

7.1 Sensitivity Analysis

As discussed in 5.3.4, a total of 100 µs after the start of the beam impact was simulated. Running this simulation this long is connected with a large computational effort (~1 d on the used computer). Therefore, to test the convergence of the result for different parameters, a shorter simulated time frame was chosen. The maximum strains appear in the impacted cross section a few 100 ns after the end of the beam impact (600 ns). Experience showed, that the important events for strain development (eg. induction of thermal strain, interaction of sample and sample holder) take place during the first 3 µs of the impact simulations.

In order to study the effects of the input parameters on the simulated I_c will be studied at a time of 3 µs after the start of the beam impact. It is assumed here, that if the simulated value converges for the moment, when the highest strains appear, it will also do so for later times when the strain has been partially released. However, this approach leads to an overestimation of the error since the error will decrease with the strain levels after the 3 µs chosen for the length of this simulation study.

7.1.1 Energy deposition

The calculated energy deposition has large influence on the simulated I_c degradation. For example: a 5 % variation in energy deposition scaling results in up to 25 % difference in relative I_c degradation for Sample 5. This parameter in a good first order approximation also includes the beam offset y_{off}, the beam cross section σ_r, the number of protons N_{p^+} and the residual Monte Carlo error of the FLUKA simulation. This is due to the fact that all these parameters alter the effective heating of the samples directly. The error on the known energy deposition in this experiment is small for areas where the energy deposition is significant. The average uncertainty in the regions of interest given by FLUKA is 2 %. The resulting relative error for the final I_c-degradation will be assumed as 10 %. Due to the lack of sample holder influence, for free samples as for samples S1, S2, and S3 the effect is not as drastic, and the final uncertainty in I_c-degradation will be assumed as 5 %.

Assuming a continuous energy deposition during the beam pulse rather than the short sub-pulses due to the bunched structure of the beam can potentially influence the development of shock waves, and may lead to different stresses and a different strain distribution.

Thus, a simulation was performed with a pulsed energy deposition. Figure 7.1 shows the difference of I_c between a continuous energy deposition and a pulsed energy deposition for sample S4 normalised. Here S4 is used instead of sample S5, because the mechanical simulation is more numerically stable. The relative error due to the difference in heating should, however, be comparable. The results show little difference between the two heating rates underlining the quasi-instantaneous nature of the experiment. A maximum error of 2.5 % was derived for the choice of a continuous energy deposition in the simulations.

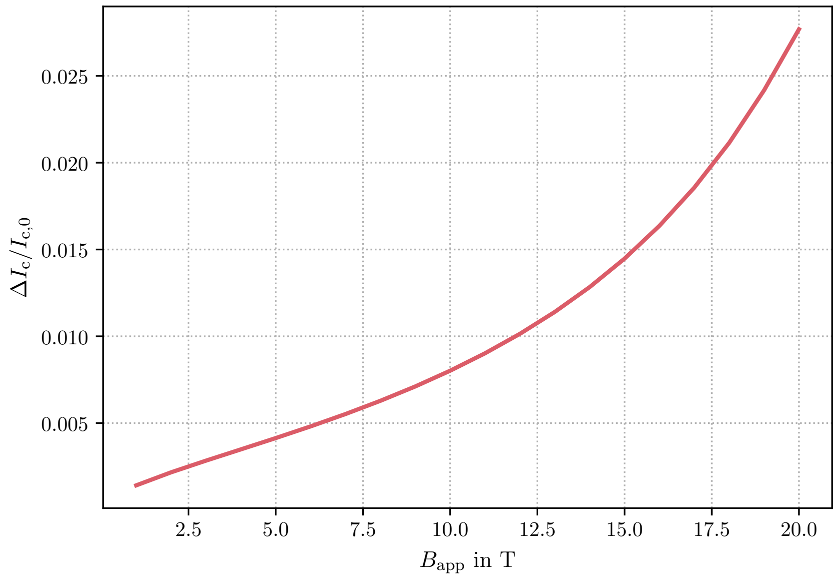

Figure 7.1: Difference in critical current I_c between continuous and pulsed energy deposition on sample S4 normalised to $I_{c,0}$ of the reference sample. This is given as a function of the applied magentic field B_{app}

7.1.2 Geometry

Slicing the sample holder has an impact on the propagation of mechanical shock waves when compared to a solid block. The used approximation uses less slices than the original geometry. To investigate the influence of this simplification, the block segment around sample 5 was simulated with all slices included. As this sample holder model was already very complex due to the number of contacts involved, the simulation did not converge anymore, when a strand was included. To still derive a quantitative result the relative displacement at the most relevant points of the groove was compared to the results with a simplified model of the sample holder. This comparison is shown in Fig.7.2. The relative difference stays below 2 %, therefore, it is reasonable to assume, that the resulting relative error in I_c is negligible. This assumption is justified, if it is taken into account, that the regions affected by this difference in groove shrinking are destroyed anyway.

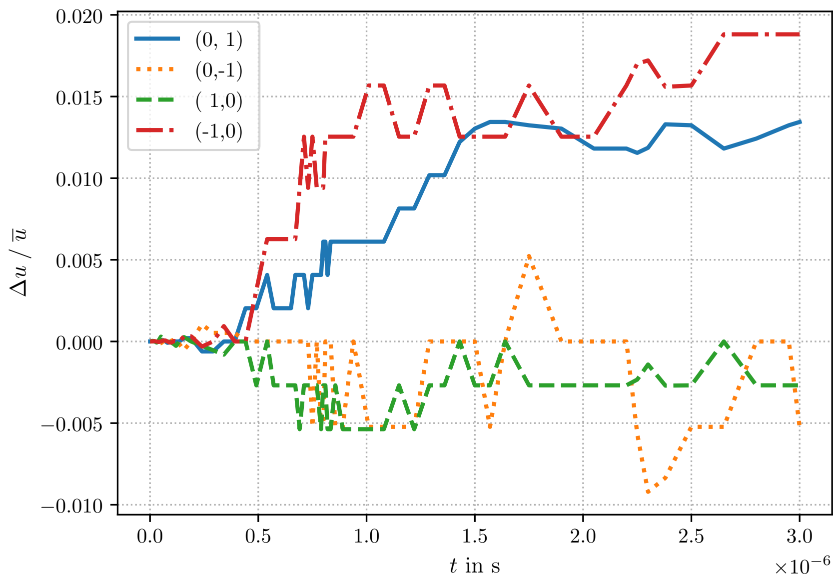

Figure 7.2: Relative displacement difference of critical points in the groove between the approximation used and sliced sample holder segment. The displacement is normalised to the average displacement. The difference is normalised to the average displacement value of the two simulations. The relevant points are on the surface of the groove. The coordinates used to identify the readout points are (y, z), with the origin in the center of the strand, z parallel to the beam axis, and y orthogonal to beam and strand. Only the displacement along the respective axes is considered.

7.1.3 Mesh Density

The mesh density changes the averaging behaviour over a given area/volume for the resulting strains. The simulated result gets closer to the real result, with increasing mesh density. Therefore, assuming a converging behaviour of the resulting I_c with increasing cross section mesh density, a study was conducted varying this parameter. The results are represented in Fig.7.3 and indicate a converging pattern above a node density of 860 nodes/mm^2. The simulated values above 860 nodes/mm^2 are fitted, assuming

$$\overline{\left(\frac{I_c}{I_{c,0}}\right)} = \alpha_1 (1 - \exp\left(\frac{\varrho_{\text{node}} - \varrho_{\text{node,ref}}}{\alpha_2}\right)) + \overline{\left(\frac{I_c}{I_{c,0}}\right)}_{\text{ref}} \quad , \tag{7.1}$$

with the mesh density ϱ_{node}. The reference values refer to the starting point of the converging pattern (mesh density of 860 nodes/mm^2), and α_i are free fit parameters.

This fit yields an actual $\overline{I_c/I_{c,0}}$ value of 0.558 , whereas the resulting value for the used density is 0.543 The choice of mesh densities was limited in such a way, that the mesh was supposed to fulfil the criteria of symmetry and equally sized mesh elements. This restriction was introduced to limit the effect of mesh related influences on the results, other than the mesh density. It cannot a priori be assumed, that this uncertainty will always result in lower I_cs. Thus, the result values are not corrected in one direction, but rather an average error in $I_c/I_{c,0}$ of 1.5 % is assumed due to a not fine enough mesh. The relative error is thus 2.7 %.

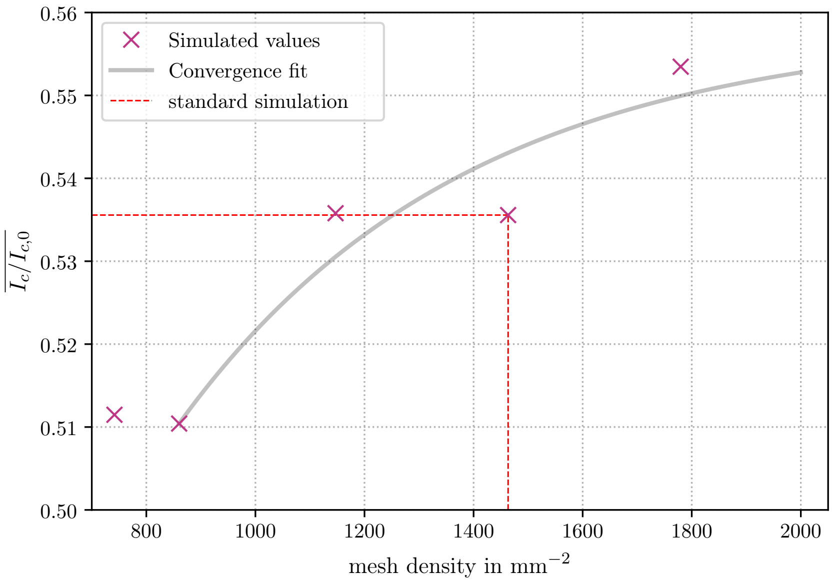

Figure 7.3: The average of the I_c degradation relative to $I_{c,0}$ over a range of $B_{app} = 5...20\,\mathrm{T}$ is shown as a function of the mesh density in the matrix region's $x = 0$ cross section. The simulated values are shown with magenta xs. The red dashed line indicates the value pair used in the standard simulation.

7.2 Systematic Uncertainties

7.2.1 Geometry Approximations

In addition to the errors resulting from the choice of geometry and mesh discussed above there are additional approximations used in the simulation, whose effect on the simulation results could only be estimated, based on experience.

Simplifying the strand's subfilament structure to a hollow cylinder region changes the systems behaviour with respect to the propagation of the deformations. This sub-filament structure absorbs the shocks induced by the sample holder in its outer layers. In the used approximations, however, the induced plastic strain is smeared out over the entire matrix region. The twisting of the sub-filaments, which was not represented in the simulations, is not expected to have any impact on the results, as the twist pitch is 14 mm. The studied region is ~1 mm and therefore hardly any twisting is present in this region. A realistic estimation for this error in I_c-degradation is in the order of 5 %. For samples without sample holder interaction, this effect will be less severe. Thus only an error in I_c-degradation of 2 % is assumed.

Other geometric approximations connected with implementing the problem in FLUKA and FEM software represent an unknown error source. A fully detailed model was not possible in the scope of the thesis and other geometric approximations that were not considered in this section could have influenced the result. For the remainder of possible I_c influencing geometry features, an error of 10 % is assumed[19].

7.2.2 Material Properties

Omitting other materials in the matrix region of the wires (as described in 5.2.1) is not a significant error in the energy deposition simulation. This is due to the fact, that the atomic percentage of the constituent elements and the average density do not change. In the thermal simulation, the influence can be mainly reduced to the local variation of C_p in the actual samples which was reduced to the overall average C_p. Therefore, super-local temperature gradients were omitted and, thus, local stresses in the first instances after impact were underestimated. These effects, however, would likely subside after a few 100 ns. Disregarding mechanically stronger phases present in the matrix region (eg. bronze) will affect the onset of plastic deformation. Since the mechanical properties of the matrix region mainly are derived from measurements on the compound material, this effect would be only marginal too. Therefore, the overall error due to omitting other materials in the matrix region will be conservatively estimated as 2 %.

Material properties over wide temperature ranges could not always be found in literature. Therefore, some properties had to be extrapolated (most importantly C_p for Nb_3Sn) or assumed constant (this is true for most mechanical properties apart from the coefficients of thermal expansion). The overall error resulting from this is estimated as 5 %.

7.2.3 Simulation Procedure

The translation of 3D-maps most importantly from FLUKA into the thermal solver of ANSYS, can cause minor aberrations because the ANSYS® mesh does not necessarily align with the binning in the FLUKA. Thus, a profile preserving interpolation between detector points is used. Because the FLUKA binning was chosen fine enough, the error would only cause a slightly higher temperature gradient on subfilament level. Therefore, an estimated resulting uncertainty in I_c-degradation of 2 % is conservative.

[19] Usually, the error of a simulation should be dominated by the geometry approximation. For FLUKA, the only geometry approximation (modelling the strands) is of a very small influence. Therefore, the non-vanishing statistical uncertainty is equally important.

The superconductor theory applied in this thesis was mostly developed for superconductors with homogeneous parameters. This study often reaches beyond the experimental verification of these models. This is especially true concerning the MAG-scaling[20]. Additionally, the used constants for the scaling relation are found for tensile measurements in axial direction. Since the principal strains in this case do not necessarily align with the axis of the strand, the scaling constants might deviate. Because the entire simulation post processing depends on these models, however, it is difficult to quantify the influence. The errors due to this are potentially large, but will not be considered in the scope of this study, since they would likely not alter the fundamental conclusions.

7.3 Resulting Confidence

Combining the above mentioned uncertainties gives a measure of the overall confidence in the simulated values for the strands relative I_c degradation.

The relative error on the simulated I_c values is given by

$$\left(\frac{\Delta I_\mathrm{c}}{I_{\mathrm{c},0}}\right)_{\mathrm{Sample}} = \sqrt{\sum_{\mathrm{relevant}} \left(\frac{\Delta I_\mathrm{c}}{I_{\mathrm{c},0}}\right)^2_{\mathrm{effect}}} \tag{7.2}$$

Which yields the values represented in Tab.7.1.

Table 7.1: Resulting uncertainties in the I_c simulations as calculated with Eqn.(7.2) considering the contributions discussed in 7.1 and 7.2.

Sample	$(\frac{\Delta I_\mathrm{c}}{I_{\mathrm{c},0}})_{\mathrm{Sample}}$ in %
S1, S2, S3	12
S4, S5, S6, S7	16
Free Samples	12

[20] This scaling is empirically tested up to ∼0.5 %. Here, the full extrapolation up to 2 % is used.

8 Comparison and Interpretation

After irradiation the samples were measured in different experiments (see 4.2). These were designed to expose the changes in critical strand parameters. In order to evaluate the simulation methodology and its results, the simulation results will be discussed and compared to the measurement data. The simulations including the sample holder did not converge for sample S8 and it could therefore not be analysed. In the experiments, however, it was still possible to measure the superconducting parameters of S8. The experimental values for S8 will be included in comparisons to indicate tendencies.

8.1 Qualitative Discussion

The critical temperature distribution, and the upper critical magnetic field could only be derived indirectly. Therefore, only a qualitative comparison of these parameters between simulated and experimental values is reasonable.

8.1.1 Bulk Critical Temperature Distributions

The direct correlation between the strain state ε_{lat} and the measurable T_{c} distribution (see Eqn.(2.12)) makes the T_{c}-density distribution a valuable way of comparing the simulation to the experiment. The measurements (see 4.2.4) were performed on the samples of batch B2. Only samples S3, S6, S8, and a reference sample(referred to as S0) were measured in this manner. Thus, the comparison is limited to the zero-strain reference, and samples S3 and S6. The comparison is shown in Fig.8.1. The measurement data was smoothed with a Gaussian filter applying a σ=77 mK. The non-smoothed Measurement Data is shown in Fig.A.9. The simulation data is given for the same sample length as the equivalent measured sample(see 5.4.6).

The wide spread of the T_{c}-density distribution towards lower values measured for sample S8 (see Fig.8.1) indicates the presence of large strains. There is no simulation data to compare this to, but it further justifies the approach of investigating residual strain as a source of I_{c} degradation.

The measurements show a small shift of the maximum in the T_{c}-density curve to higher temperatures for sample S3 and to lower temperatures for samples S6 and S8 as compared to the reference sample. This behaviour is well reproduced in the simulation, showing an even stronger shift of the peak.

The shape of the reference T_{c}-density distribution is not perfectly represented by a Gaussian distribution, but is slightly skewed. The density maxima are systematically shifted to higher values in the simulation data. Also, the reference sample in the measurements exhibits a tail towards lower T values, which is not reproduced by the Gaussian profile. Both samples S3 and S6, however, develop the shape of a Gaussian slightly skewed towards higher temperatures.

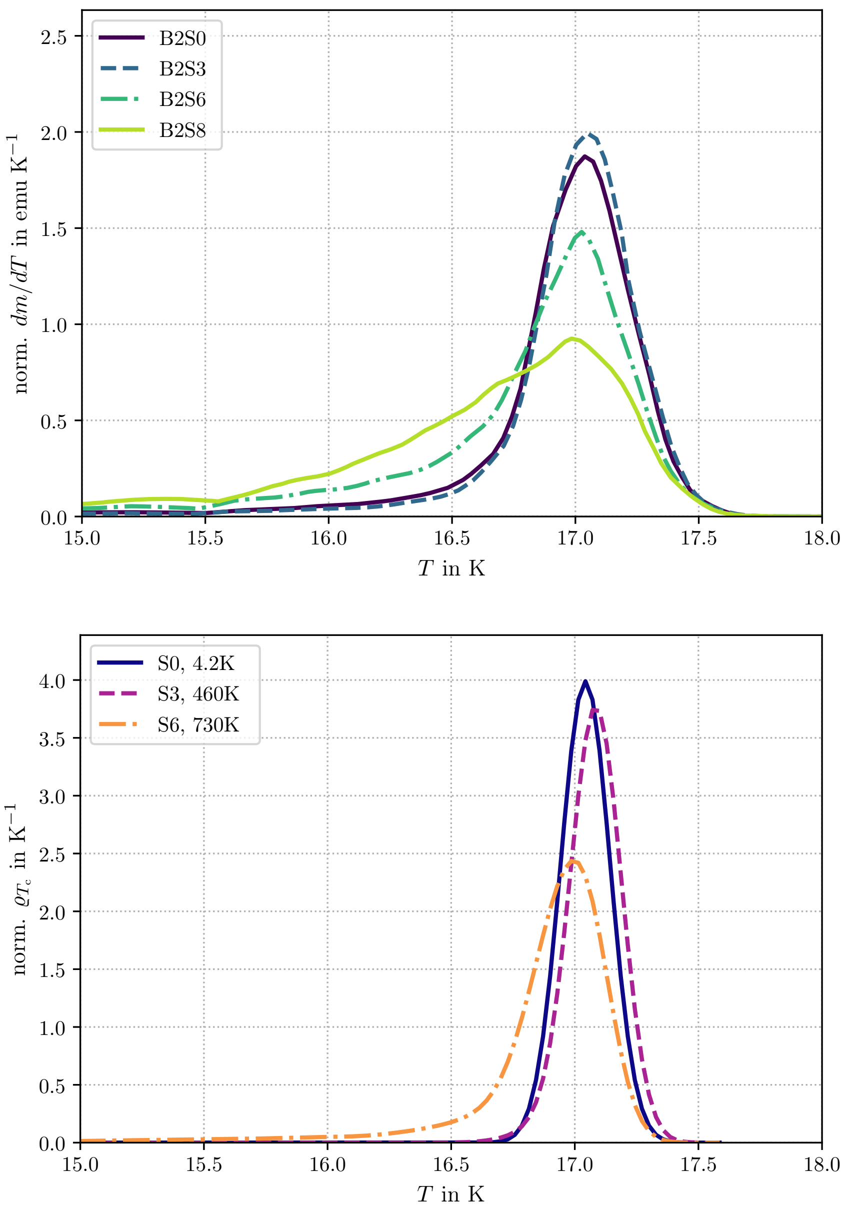

Figure 8.1: Comparison of critical temperature density ϱ_{T_c} profiles over temperature T in the samples. The plot on the top shows the measured change of magnetisation with temperature. The bottom plot shows the density of critical temperature ϱ_{T_c} as taken from the simulations.

In the measurements, the peak for sample S3 is higher than the one of the reference sample. This behaviour cannot be reproduced by the applied simulation method, as the T_c-density distribution cannot become narrower than the reference curve and the integral is kept constant. However, the tails of the distribution are similar to the reference sample, which is also reproduced in the simulations.

For Sample S6, the width of the simulated curve is closer to that of the measured curve than for S3 and the reference. This is because for wider spreads in the non-filtered simulated T_c-density distribution, the initially assumed shape is reflected less in the result. The measurements exhibit a larger tail for sample S6 towards lower values of T. This is reproduced by the simulation data with respect to the simulated reference curve.

The measurements could only be done for a - compared to the expected size of the degraded zone - larger volume. Fig.6.1 shows a monotonous dependence of T_c distribution change with hotspot temperature. The dependence (unlike for example the I_c degradation) is not disrupted by Sample 5, or Sample 7. This shows, that the bulk degradation of the sample cutout is not necessarily the same as that of the super localised cross section degradation (responsible for I_c degradation). It is, however still a valuable parameter to validate the simulation with.

8.1.2 Critical Field Extrapolations

The extrapolation of B_{c2} from an $I_c(B_{app})$ curve depends strongly on the overall shape of the curve. It can thus be seen as a measure of the relative curve shape. This is mainly determined by baseline strain on the Nb_3Sn. Fig.8.2 compares of the B_{c2} values which were extrapolated from Kramer fits of I_c data given in Fig.6.2 and Fig.6.6, and the measured I_c values of batch B1. The orange triangles are the results of a simulation assuming only strain depend I_c degradation. The purple triangles show the simulation results including the cracking of parts of the filaments. The green circles show the B_{c2} as derived from I_c measurements of the sample from batch B1.

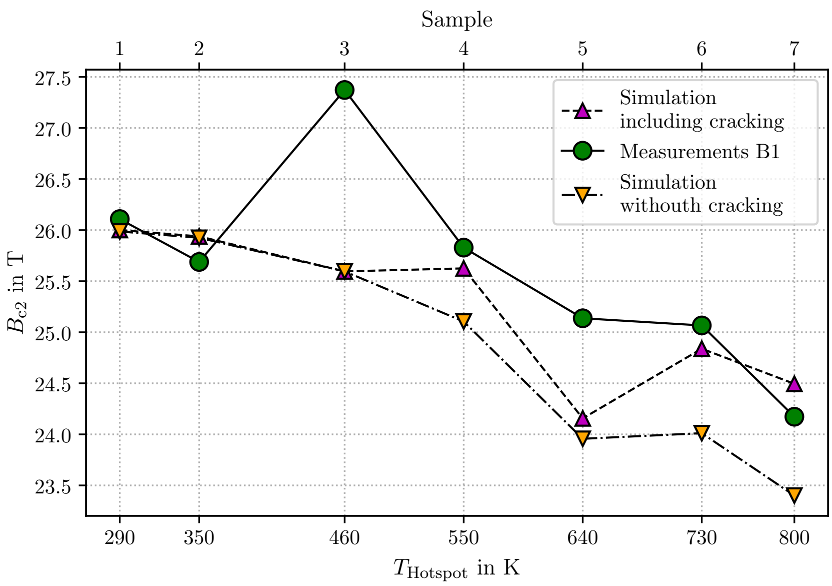

Figure 8.2: Comparison of B_{c2} as function of the hotspot temperatures between simulations and measurement data of Batch 1. Linear interpolations between data points were included for better comparability.

The measurement data shows no strong change in the extrapolated B_{c2} for Sample S1, S2 and S4. A slight discontinuity in the measurement of sample S3 changed the extrapolated value significantly, so that the S3 strays from a value one would expect from interpolation. Samples S5, and S6 B_{c2} form a plateau lower than the first. Sample S7 then exhibits a significant drop.

In both simulations, the extrapolated B_{c2} values decrease with hotspot temperature. The relative tendencies given by the measurements are well reproduced by the simulation not including cracking. The absolute values however are shifted towards lower values. This indicates that the baseline strain is indeed responsible for the relative shift in extrapolated B_{c2}. The simulated values for which cracking was considered is closer to the absolute values derived from the measurements. This is because, without cracking, the filaments under high strain are still regarded to carry current at lower magnetic fields, lifting I_c in this range. This gives the fit a steeper slope and results in lower values for the extrapolation. The cracking thus needs to be taken into account. Since there is little cracking expected in Sample 5 the B_{c2} value remains low for the simulation including the cracking too.

As can be seen later in Fig.8.4 and Fig.8.5 the simulated I_c values for high magnetic fields are systematically lower than the measured ones[21]. This is likely an experimental effect due to relatively small currents in this regime. The small offset in I_c degradation results in a discrepancy when extrapolating the data. This is because in the Kramer form, the values are weighed with $B^{\frac{1}{2}}$ giving larger importance those in the high field regime. The results for the simulation including the cracking are thus slightly lower than those derived from the measurements.

8.2 Quantitative Comparison

The strands' critical current as a function of the magnetic field was directly measured. Thus, these values can be compared quantitatively. Additionally, the influence of the sample holder will be shown in this section by comparing simulated critical current results.

8.2.1 Influence of the Sample Holder

Understanding the contribution of the sample holder deformation due to the beam impact on the degradation of the properties of the strand samples is important for the correct interpretation of the measurement results and their extrapolation to magnets in an accelerator. Figure 8.3 shows the simulated critical current variation of the samples as a function of the hotspot temperature for an external field of 5 T (top) and 19 T (bottom). The blue triangles indicate the simulation results for free strands and the orange triangles for the samples installed within the sample holder. The I_c values are normalised to a self field corrected equivalent zero strain strand. The hotspot temperature is calculated for pure copper.

[21] This is true apart from sample S7, where this argumentation, hence, doesn't apply.

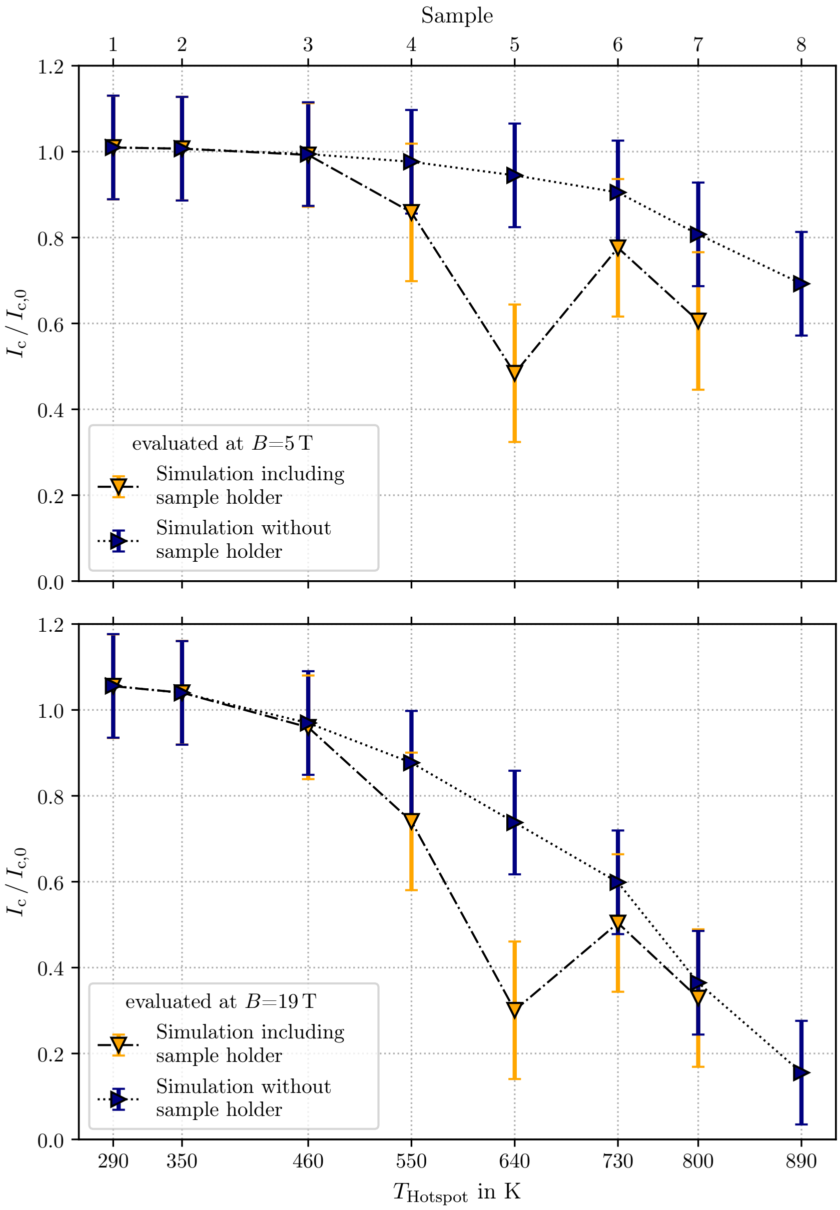

Figure 8.3: Simulated critical current variation of the samples as function of the hotspot temperature for an external field of 5 T (top) and (19 T (bottom).

The minimal strain in the impacted strand cross section increases with increasing hotspot temperature T_{Hotspot}, leading to a degradation of the critical current I_c in both cases. Samples S1 to S3 do not interact with the sample holder. Thus, there is no observable difference in the results between the two simulations.

From sample S4 onward the effect of the sample holder is strongly visible. It causes a 12 % (13 %) stronger degradation of I_c at an external field of 5 T (19 T). This is due to the fact, that the sample holder squeezes a small part of the strand's matrix region due to its deformation after the beam impact. The filaments in this region are completely destroyed and therefore do not carry any current.

The effect of the sample holder on the degradation of the critical current is strongest for sample S5. This can be explained by its position in the sample holder. Therefore, I_c is degraded 43 % more than expected for a free strand with the same beam impact.

For samples S6 and S7 the difference between the free strand case and the case with sample holder is smaller at an external field of 19 T than at 5 T. The differences are 13 % (S6) and 20 % (S7) at 5 T and 9 % and 4 % at 19 T. This is due to an overlap between regions strongly affected by both directly beam (from now on intrinsic), and sample holder induced (from now on extrinsic) degradation. For weaker magnetic fields the subfilaments affected by the weaker intrinsic degradation still carry large currents. Since I_c scales significantly with $b = \frac{B}{B_{c2}(\varepsilon_{lat})}$, the current carried by these regions drops considerably already before $B_{c2,0}$. For higher B_{app} the I_c degradation depends more on the base line degradation rather than the maximum values. The baseline degradation is mostly determined by intrinsic effects. Therefore, the relative I_c degradation in higher fields is more similar for the two simulation types than in lower fields.

For samples with no sample holder interaction (S1, S2, S3), there is no difference in relative I_c. For the samples of weak sample holder interaction (S4, S6, S7) the difference between the simulations are mostly within the respective error bars for. For S4, however the Sample holder needs to be taken into account as a damage source for all magnetic fields strengths. A significant difference in degradation is observable for strong sample holder interaction (S5[22]).

8.2.2 Comparison with Critical Current Measurements

Figure 8.4 and Fig.8.5 show the relative degradation of the critical current in dependence of hotspot temperature. The green dots represent the measured degradation relative to the data expected for a non-impacted sample. The measurements are the average between the measured batches B1 and B2. The relative error on the measurements are a working estimate until the final release of the study summary [32]. The yellow triangles represent the simulated I_c degradation without taking cracking as a damage mechanism into account. The purple triangles represent the simulated data including filament cracking as a damage mechanism. The values are shown for a weak (5 T) and a strong (19 T) magnetic field. Additionally, two magnetic field strengths characteristic for the HL-LHC (11 T and 16 T) are considered. For some of the relevant field values measurements are not available.

For measurements and simulations alike, Fig.8.4 and Fig.8.5 show a significant drop-off in critical current above 550 K (sample S4) for all magnetic fields. For the measurements and the simulation including cracking, two separate clusters form, where S1-S3 show little to no degradation (or even improvement), and S4-S7 are severely degraded. This

[22] This would likely be the case for S8 too. But since the simulation did not converge, there is no data to investigate this claim by.

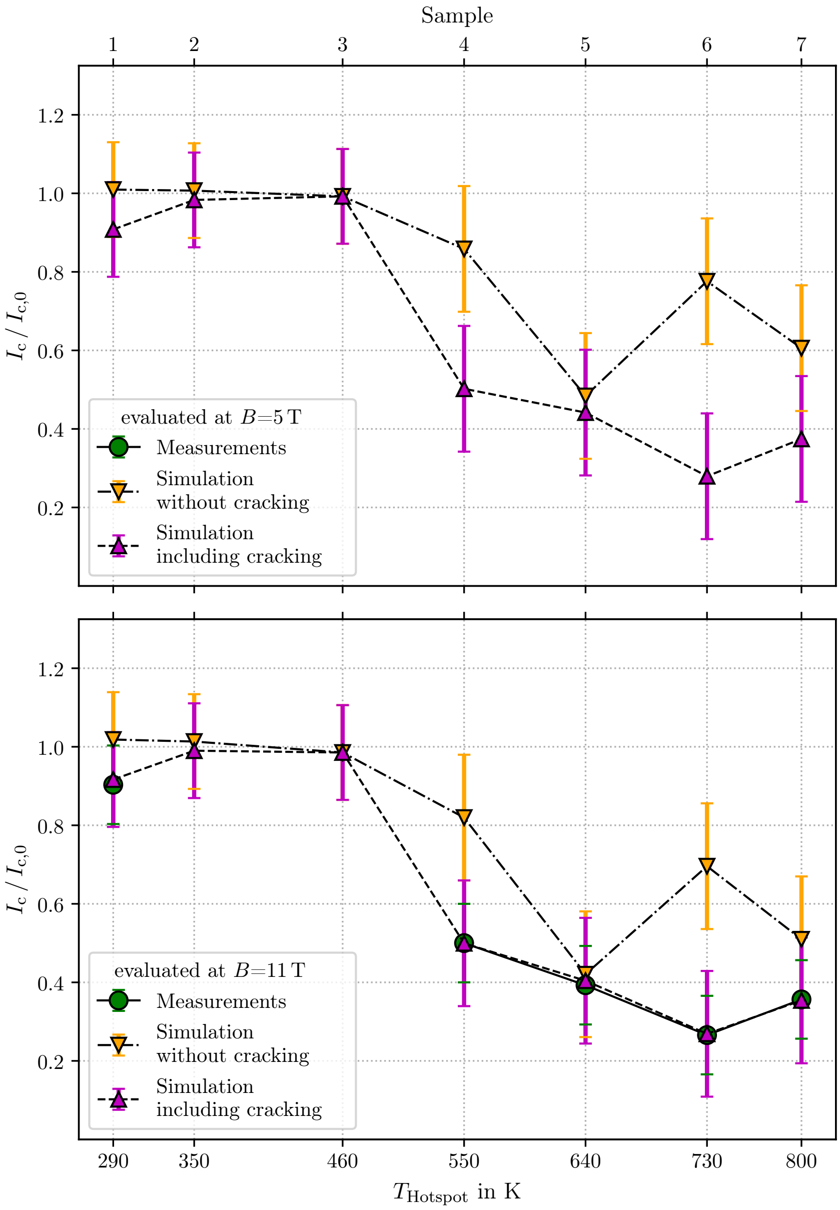

Figure 8.4: Degradation of the critical current relative to an undegraded sample in dependence of hotspot temperature. Comparison between simulation and measurement data for important magnetic field strengths in the 5...20 T range.

onset of severe degradation coincides with the onset of sample holder influence in Fig.8.3. However, the severity of the onset cannot be explained by the mild sample holder influence on S4 (see no-cracking simulation in Fig.8.4 and Fig.8.5). Therefore, the onset must be explained by a separate mechanism (filament cracking).

For all samples, the measured $I_c(B_{\text{app}})$ is well reproduced by the simulation model including the cracking mechanism. The difference between the simulations not including cracking and the measurements and the simulations including cracking is prominent for

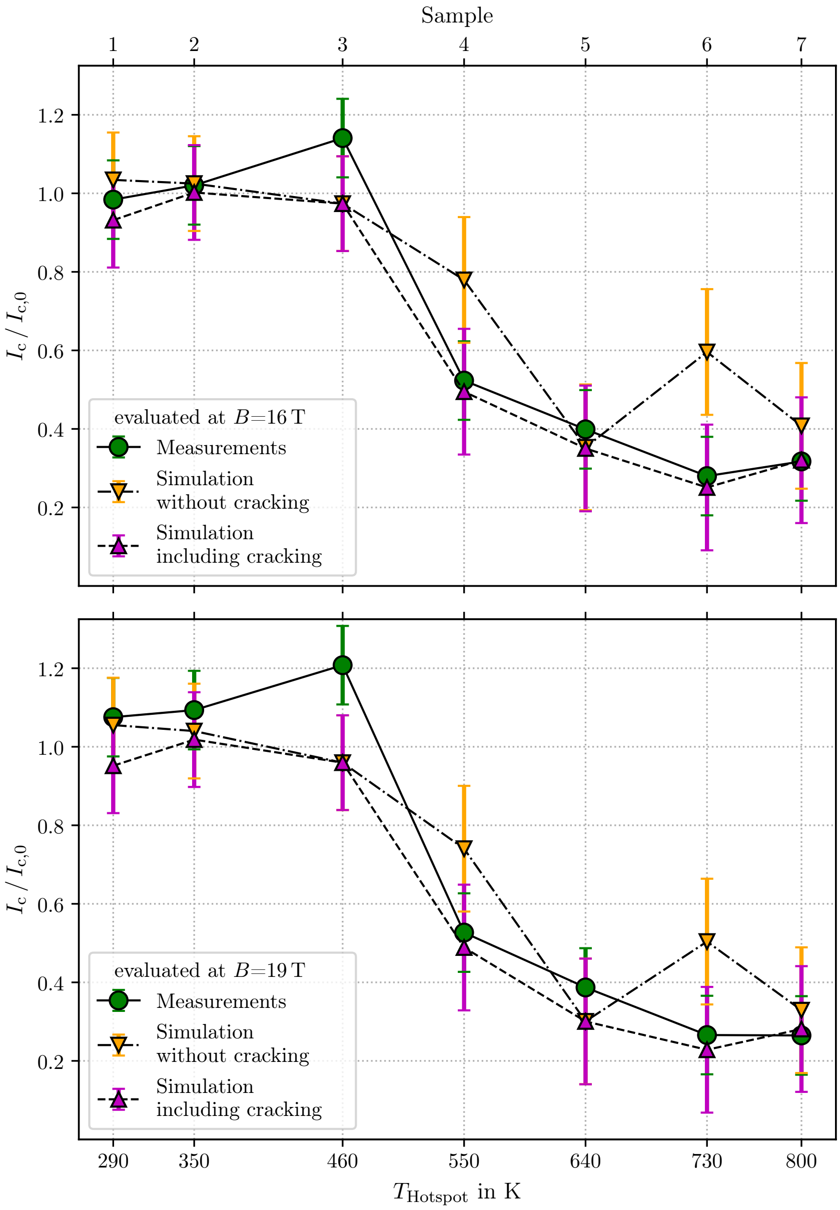

Figure 8.5: Degradation of the critical current relative to an undegraded sample in dependence of hotspot temperature. Comparison between simulation and measurement data for important magnetic field strengths in the 5...20 T range.

S4, S6 and S7 for weaker magnetic fields, but decreases for stronger ones.

For strong magnetic fields, the measurements for the samples exposed to a small energy deposition (namely S1, S2 and S3) show a significant increase in relative I_c. An improvement of this magnitude can not be explained with the simulation data within reasonable bounds of the used theory, and is thus not reproduced in the simulations.

From the difference between the simulations including filament cracking and those that do not conclusions can be made to the expected influence of filament cracking for each sample. The expected influence of filament cracking in the samples is thus:

For samples S1 to S3, no cracking is expected. The cracking algorithm artificially tries to reproduce the initial rise in I_c in the measurement data. The resulting I_c difference for sample S1 is 10 % for all magnetic fields. For S2 the values defer by 2 %, and for S3 not at all. The magnetic field independence of the difference is due to the small degradation of these samples. Hence, the constant cracking multiplier applied to the different nodes always applies to more or less ideally conducting nodes.

For sample S4 a strong influence of cracking is expected from the simulations. Including cracking and not doing so yields results differing by 45 % at 5 T and 22 % at 19 T. For S6 this difference is 50 % at 5 T and 27 % at 19 T. For S7 it lies between 23 % at 5 T and 5 % at 19 T.

For sample S5, the degradation due to residual strain already matches the measurements. Therefore, the algorithm avoids adding any extra degradation due to filament cracking (see Fig.A.7). The difference in relative I_c degradation is here, 4 % at 5 T and 0 % at 19 T.

8.3 Interpretation

The simulations allowed to identify the two dominating mechanisms causing the observed degradation of the critical current as a function of the hotspot temperature in the strand samples. The first mechanism is the cracking of filaments around the beam impact zone. The second is a plastic deformation of the copper matrix causing residual strains in the Nb_3Sn filaments. The latter effect was further supported by magnetisation measurements performed on a few samples, which allowed to estimate the degradation of the critical temperature, which is expected to be caused by this mechanism.

The share of both mechanisms in the observed degradation of critical current varies with hotspot temperature. For low hotspot temperatures (up to ∼460 K in Cu) no filament cracking was assumed. For samples S4, S6, and S7 (hotspot temperature of 550 K, 640 K and 800 K in Cu respectively) a significant part of the observed degradation is due to filament cracking. In sample 5 (640 K in Cu) -due to the strong sample holder interaction-both effects have a significant influence. Samples S8, S9, and S10 could not be simulated due to the severity of the sample holder interaction. For these samples, both sources are, thus, expected to have a significant influence due to the severity of the sample holder influence.

The simulations showed, that already for low hotspot temperatures (beginning already with S1, 290 K in Cu) plastic deformation occurs due to the very localised shock heating caused by the beam. The presence of residual strain in the Nb_3Sn phase was indicated by the drop of bulk B_{c2} measured in the strands with hotspot temperature, and confirmed by magnetisation measurements. For hotspot temperatures up to ∼460 K in Cu, no change in critical current could be resolved, due to the uncertainties of the experimental methods. Thus, the understanding of the dominating damage mechanisms is here purely dependent on simulations. Further experiments would be needed to validate the simulation results. The method applied proved capable of describing the degradation of samples in the range up to ∼800 K in Cu. However, describing strand degradation that involves large movement makes simulations less reliable (S5) or even impossible (S8).

The mismatch in bulk I_c and B_{c2} measured indicated another damage mechanism. The mechanism of filament cracking is well know for Nb_3Sn. Its presence was confirmed for hotspot temperatures above 550 K in Cu through additional microscopic studies on several samples. The onset of filament cracking was identified by the simulations at S4 (550 K in Cu), and could not be observed in S3 (460 K in Cu). With a reasonable safety margin, filament cracking can be expected in Nb_3S strands from ∼450 K in Cu for a focused proton beam. Above this temperature filament cracking becomes the dominant degradation mechanism.

As magnets in the LHC are usually run at their maximum current capacity, already small degradations in I_c are critical. Therefore, hotspot temperatures above ∼450 K should be avoided in Nb_3Sn strand based magnets to ensure nominal function.

9 Outlook

With the presented model it was possible to describe the damage mechanisms in Nb_3Sn. As part of the experiment, two other superconductor types (Nb-Ti and YBCO) were irradiated under the same conditions.

The Nb-Ti strands, however, were already conclusively analysed experimentally [6].

The YBCO tapes are currently being analysed, and can likely be simulated in the same way as the Nb_3Sn strands. This requires a reliable strain scaling function for YBCO tapes. Such a function is, due to the relative novelty of the material, not as much of a consensus gentium as for the Nb_3Sn. Due to the fact, that the YBCO tapes were fixed in the sample holder, the method should be applicable to all samples.

The original intend of this study was to identify the onset of degradation in the Nb_3Sn strands. This onset was identified in the experiment and by the simulations for sample S4. In order to further pinpoint the exact conditions leading to the onset of degradation, future experiments should lay focus on this regime.

The simulations discussed in this thesis and the associated experiment were based on the strands, that would be wound into coils for the magnets. Based on the findings of this study, it would be reasonable, to stage an experiment in the hotspot regime around 400...600 K, with small coils as a target. Such a follow-up experiment is currently being prepared in collaboration with the Karlsruhe Institute of Technology.

So far only relatively simple geometries were analysed with the simulation method described in this thesis. To safely rely on the simulations to evaluate damage to the complex magnets in the HL-LHC, the method would have to be validated on more complex geometries like the coils in the follow-up experiment.

If the follow-up experiment reproduces the findings of this study, an experiment on a full scale magnet coil will be feasible to finalise the study.

Bibliography

[1] *CERN panoramas outreach.* https://panoramas-outreach.cern.ch/static/media/cern-complex.51240. Accessed: 2020-03-16.

[2] *CERN about CERN.* https://home.cern/about. Accessed: 2020-03-16.

[3] Oliver Brüning and Lucio Rossi. *The High Luminosity Large Hadron Collider.* 1st ed. WORLD SCIENTIFIC, 2015. DOI: 10.1142/9581. eprint: https://www.worldscientific.com/doi/pdf/10.1142/9581. URL: https://www.worldscientific.com/doi/abs/10.1142/9581.

[4] I. Béjar Alonso et al. *High-Luminosity Large Hadron Collider.* Tech. rep. CERN, Sept. 2017.

[5] Vivien Raginel. "Study of the Damage Mechanisms and Limits of Superconducting Magnet Components due to Beam Impact". Presented 04 Jul 2018. PhD thesis. June 2018. URL: https://cds.cern.ch/record/2628622.

[6] A. Will et al. "Beam Impact Experiment of 440GeV/p Protons on Superconducting Wires and Tapes in a Cryogenic Environment". In: *Proc. 10th International Particle Accelerator Conference (IPAC'19), Melbourne, Australia, 19-24 May 2019* (Melbourne, Australia). International Particle Accelerator Conference 10. https://doi.org/10.18429/JACoW-IPAC2019-THPTS066. Geneva, Switzerland: JACoW Publishing, June 2019, pp. 4264–4267. ISBN: 978-3-95450-208-0. DOI: doi:10.18429/JACoW-IPAC2019-THPTS066. URL: http://jacow.org/ipac2019/papers/thpts066.pdf.

[7] Anton Lechner. "Particle interactions with matter". In: *CERN Yellow Reports: School Proceedings* 5.0 (2018), p. 47. ISSN: 2519-805X. DOI: 10.23730/CYRSP-2018-005.47. URL: https://e-publishing.cern.ch/index.php/CYRSP/article/view/714.

[8] Peter Sigmund. *Particle Penetration and Radiation Effects.* Springer Berlin Heidelberg, 2006. DOI: 10.1007/3-540-31718-x. URL: https://doi.org/10.1007/3-540-31718-x.

[9] M. J. Berger et al. "Report 49". In: *Journal of the International Commission on Radiation Units and Measurements* os25.2 (Apr. 2016), NP–NP. ISSN: 1473-6691. DOI: 10.1093/jicru/os25.2.Report49. eprint: https://academic.oup.com/jicru/article-pdf/os25/2/NP/9587198/jicruos25-NP.pdf. URL: https://doi.org/10.1093/jicru/os25.2.Report49.

[10] A. Ferrari and P.R. Scala. "Proceedings of the Workshop Nuclear Reaction Data and Nuclear Reactors". In: *Nuclear Reaction Data and Nuclear Reactors.* Ed. by A. Gandini and G. Reffo. WORLD SCIENTIFIC, May 1998. DOI: 10.1142/9789814530385. URL: https://doi.org/10.1142/9789814530385.

[11] Y. Nie et al. "Numerical simulations of energy deposition caused by 50 MeV—50 TeV proton beams in copper and graphite targets". In: *Phys. Rev. Accel. Beams* 20 (8 Aug. 2017), p. 081001. DOI: 10.1103/PhysRevAccelBeams.20.081001. URL: https://link.aps.org/doi/10.1103/PhysRevAccelBeams.20.081001.

[12] J. File and R. G. Mills. "Observation of Persistent Current in a Superconducting Solenoid". In: *Phys. Rev. Lett.* 10 (3 Feb. 1963), pp. 93–96. DOI: 10.1103/PhysRevLett.10.93. URL: https://link.aps.org/doi/10.1103/PhysRevLett.10.93.

[13] Michael Tinkham. *Introduction to Superconductivity.* 2nd ed. Dover Publications, June 2004. Chap. 5. ISBN: 0486435032.

[14] Kyojim Tachikawa and Peter J. Lee. In: *100 years of superconductivity.* Ed. by Horst Rogalla and Peter H. Kes. 1st ed. CRC Press, Nov. 2011. Chap. 10. ISBN: 9781439849460.

[15] Edward J. Kramer. "Scaling laws for flux pinning in hard superconductors". In: *Journal of Applied Physics* 44.3 (1973), pp. 1360–1370. DOI: 10.1063/1.1662353. eprint: https://doi.org/10.1063/1.1662353. URL: https://doi.org/10.1063/1.1662353.

[16] A Godeke et al. "A general scaling relation for the critical current density in Nb3Sn". In: *Superconductor Science and Technology* 19.10 (Sept. 2006), R100–R116. DOI: 10.1088/0953-2048/19/10/r02. URL: https://doi.org/10.1088%2F0953-2048%2F19%2F10%2Fr02.

[17] Arno Godeke et al. "Characterization of High Current RRP Wires as a Function of Magnetic Field, Temperature, and Strain". In: *Applied Superconductivity, IEEE Transactions on* 19 (July 2009), pp. 2610–2614. DOI: 10.1109/TASC.2009.2018473.

[18] A Nijhuis, Y Ilyin, and W Abbas. "Axial and transverse stress–strain characterization of the EU dipole high current density Nb3Sn strand". In: *Superconductor Science and Technology* 21.6 (Mar. 2008), p. 065001. DOI: 10.1088/0953-2048/21/6/065001. URL: https://doi.org/10.1088%2F0953-2048%2F21%2F6%2F065001.

[19] B Bordini et al. "An exponential scaling law for the strain dependence of the Nb3Sn critical current density". In: *Superconductor Science and Technology* 26.7 (May 2013), p. 075014. DOI: 10.1088/0953-2048/26/7/075014. URL: https://doi.org/10.1088%2F0953-2048%2F26%2F7%2F075014.

[20] D. R. Chichili et al. In: *Proceedings of the 1999 Particle Accelerator Conference, New York.* 1999, pp. 3342–3344.

[21] Najib Cheggour et al. "Implications of the strain irreversibility cliff on the fabrication of particle-accelerator magnets made of restacked-rod-process Nb3Sn wires". In: *Scientific Reports* 9.1 (Apr. 2019), p. 5466. ISSN: 2045-2322. DOI: 10.1038/s41598-019-41817-7. URL: https://doi.org/10.1038/s41598-019-41817-7.

[22] P. Ferracin et al. "Development of MQXF: The Nb_3Sn Low-β Quadrupole for the HiLumi LHC". In: *IEEE Trans. Appl. Supercond.* 26.4 (June 2016), p. 4000207. DOI: 10.1109/TASC.2015.2510508.

[23] Matthew. C. Jewell. "The effect of strand architecture on the fracture propensity of Nb3Sn composite wires". PhD thesis. University of Wisconsin, 2008, pp. 79, 87.

[24] Russel E. Caflisch. "Monte Carlo and quasi-Monte Carlo methods". In: *Acta Numerica* 7 (1998), pp. 1–49. DOI: 10.1017/S0962492900002804.

[25] *FLUKA about FLUKA.* http://www.fluka.org/fluka.php?id=about&mm2=1. Accessed: 2020-02-20.

[26] T.T. Böhlen et al. "The FLUKA Code: Developments and Challenges for High Energy and Medical Applications". In: *Nuclear Data Sheets* 120 (2014), pp. 211–214. ISSN: 0090-3752. DOI: https://doi.org/10.1016/j.nds.2014.07.049. URL: http://www.sciencedirect.com/science/article/pii/S0090375214005018.

[27] Giuseppe Battistoni et al. "Overview of the FLUKA code". In: *Annals Nucl. Energy* 82 (2015), pp. 10–18. DOI: 10.1016/j.anucene.2014.11.007.

[28] Jean-Michel Bergheau and Roland Fortunier. *Finite Element Simulation of Heat Transfer*. Jan. 2008. ISBN: 9781848210530. DOI: 10.1002/9780470611418.part1.

[29] ANSYS Inc. *Theory Reference for the Mechanical APDL and Mechanical Applications*. Apr. 2009, pp. 181–186.

[30] Andreas Oslandsbotn. *Internal Note: Beam Impact on Superconductor short samples of Nb_3Sn, Nb-Ti and YBCO*. Tech. rep. CERN, Dec. 2018.

[31] Andreas Will et al. "Impact of 440 GeV Proton beams on Superconductors in a Cryogenic Environment". In: *Proceedings of the 14th European Conference on Applied Superconductivity*. IOP Science, 2019 forthcoming. URL: https://iopscience.iop.org/journal/1742-6596/page/www.eucas2019.org.

[32] Andreas Will. "Damage mechanisms in superconducting particle accelerator magnets due to the impact of high energy particles (preliminary title)". PhD thesis. Karlsruher Institut für Technologie (KIT), 2020 forthcoming.

[33] N. J Simon, E. S. Drexler, and R. P. Reed. *Properties of Copper and Copper Alloys at Cryogenic Temperatures*. Boulder, Colorado: National Bureau of Standards, Feb. 1992, p. 717.

[34] Malcom W. Jr. Chase. *NIST-JANAF Themochemical Tables*. 4th ed. 9. Gaithersburg, Maryland: National Institute of Standards and Technology, 1998, p. 1005. ISBN: 1-56396-819-3.

[35] Gwendowlyn S. Knapp, Samuel D. Bader, and Zachary Fisk. "Phonon properties of A-15 superconductors obtained from heat-capacity measurements". In: *Physical Review B* 13.9 (May 1976). ISSN: 0163-1829.

[36] Yingxu Li and Yuanwen Gao. "GLAG theory for superconducting property variations with A15 composition in Nb_3Sn wires". In: *Scientific Reports* 7.1 (2017), p. 1133. ISSN: 2045-2322. DOI: 10.1038/s41598-017-01292-4. URL: https://doi.org/10.1038/s41598-017-01292-4.

[37] M. N. Khlopkin. "The specific heat of Nb3Sn in magnetic fields up to 19 T". In: *Sov. Phys. JETP* 63.1 (Jan. 1986). ISSN: 0044-4510.

[38] Jose Ferradas et al. "Electromechanical characterization of Nb_3Sn conductors at University of Geneva". In: Workshop on Nb_3Sn technology for accelerator magnets (Paris, France, Espace St Martin, Oct. 11–12, 2018). CERN and CEA Saclay. 2018. URL: https://indi.to/YhZGL.

[39] H. Devantay et al. "The physical and structural properties of superconducting A15-type Nb-Sn alloys". In: *Journal of Materials Science* 16.8 (Aug. 1981), pp. 2145–2153. ISSN: 1573-4803. DOI: 10.1007/BF00542375. URL: https://doi.org/10.1007/BF00542375.

[40] P. Bauer and H Rajainmaki. *Material Data Compilation for Superconductor Simulation*. Tech. rep. EFDA, Apr. 2007.

[41] J. G. Hust and A. B. Lankford. *Thermal conductivity of aluminium, copper, iron, and tungsten for temperatures from 1 K to the melting point*. Boulder, Colorado: National Bureau of Standards, July 1984, pp. 28–29.

Appendix

A Complementary Plots

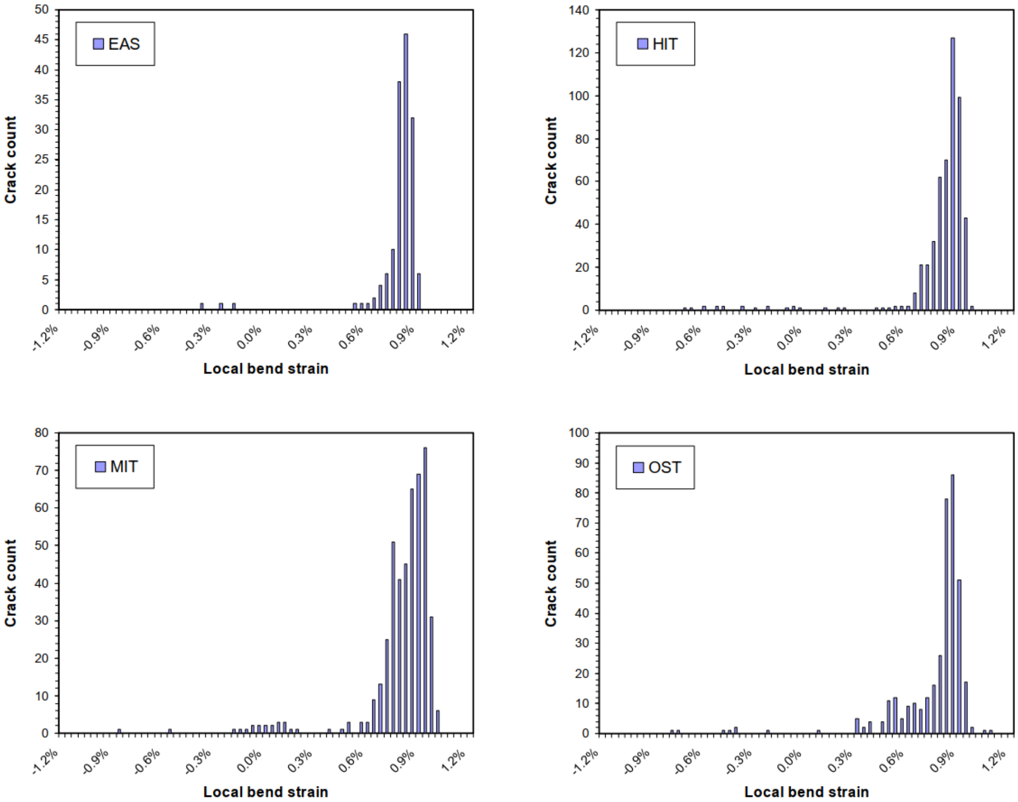

Figure A.1: Distribution of fracture events as a function of bend strain in Nb_3Sn strands (i)EAS, (ii)Hitachi, (iii)Mitsubishi, (iv)Oxford(now Bruker) ITER
Taken from Jewell [23]

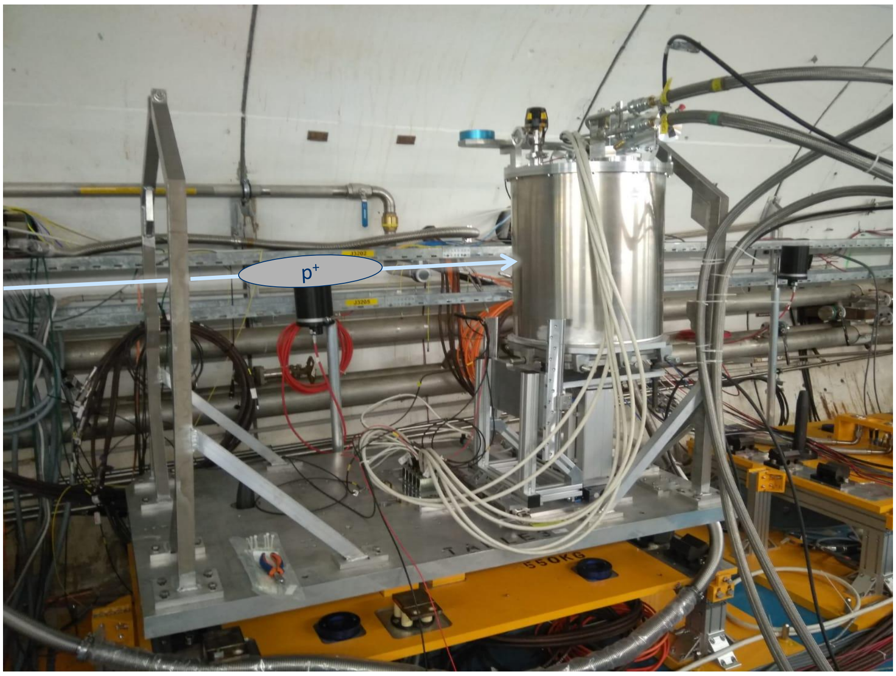

Figure A.2: Experimental setup in HiRadMat: cryostat on table with schematic proton path

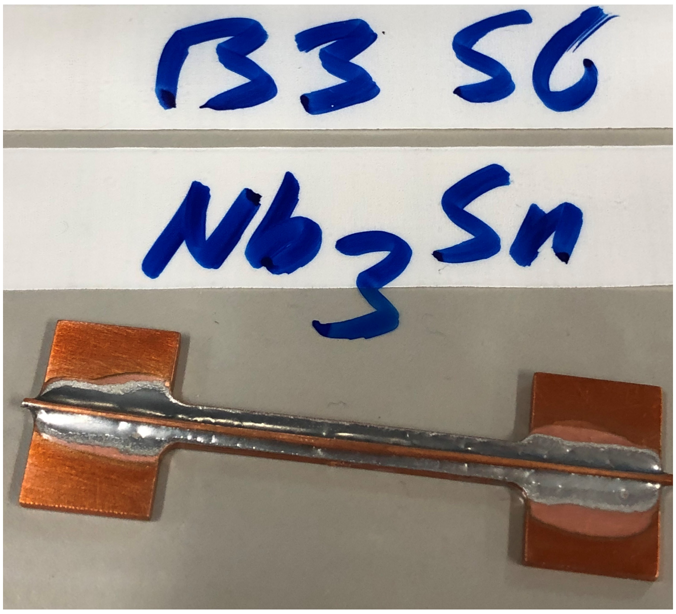

Figure A.3: Nb_3Sn Sample Batch 3 Sample 6 soldered onto the supporting dog bone, prepared for I_c measurement

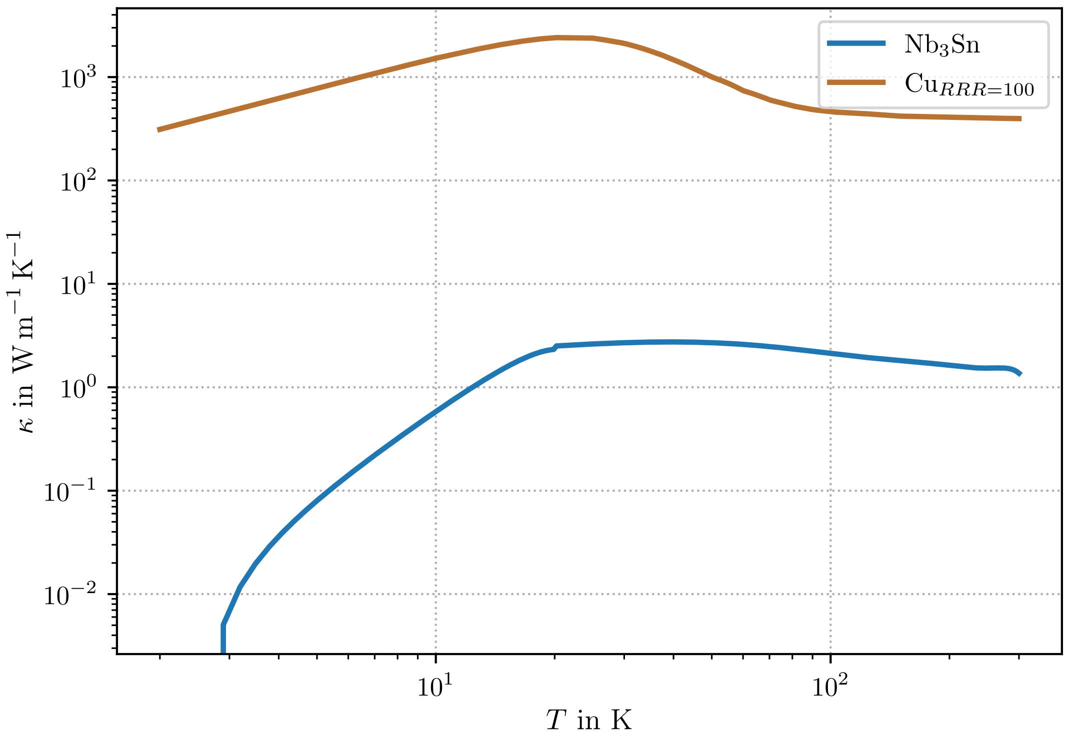

Figure A.4: Comparison of thermal conductivity κ as a function of temperature T for Nb_3Sn [40] and $Cu_{RRR=100}$ [41]

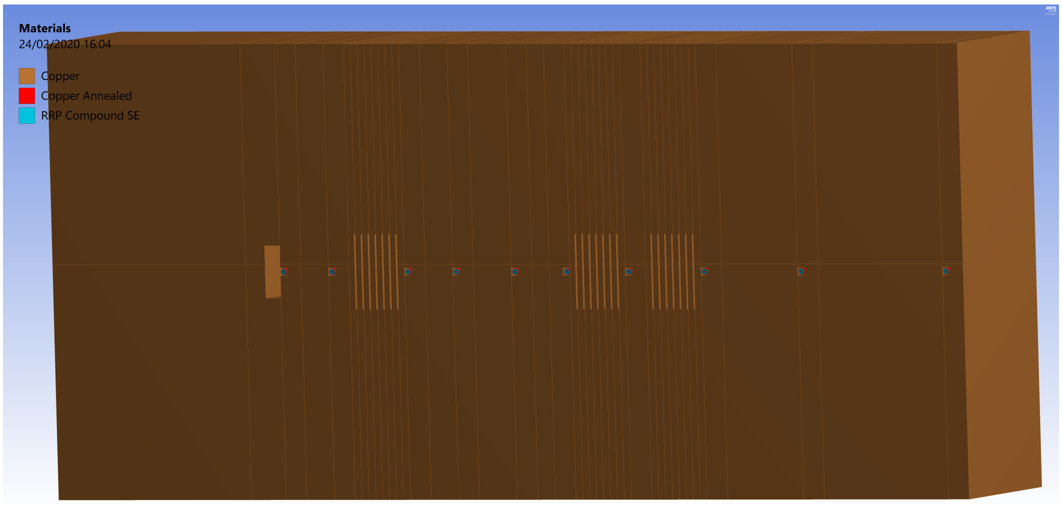

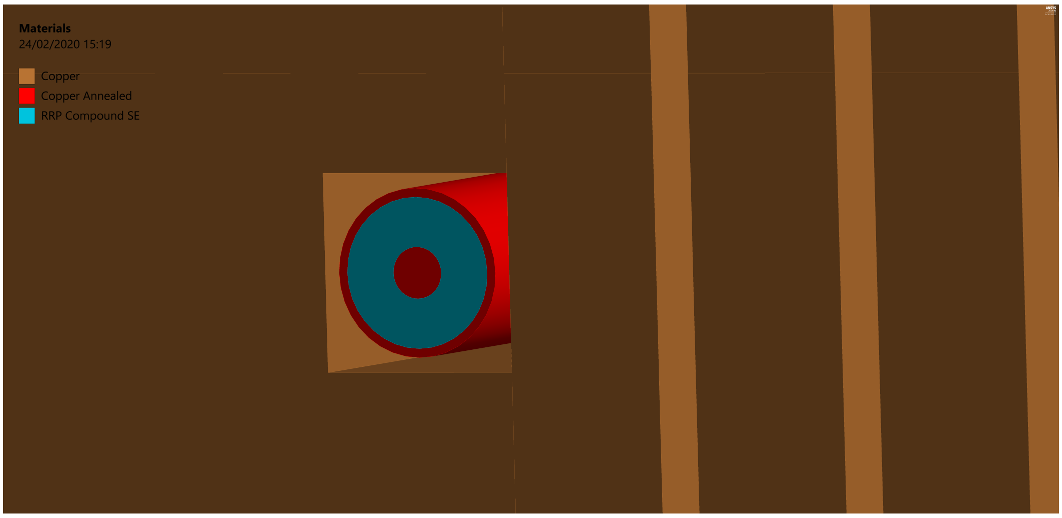

Figure A.5: The geometry approximation used for the thermal simulation shown in overview and S6 exemplary in close up.
The iron restrictions are not modelled; the strands are modelled in the concentric cylinder model; vacuum grease and temperature detecting metal foils are omitted.
Cold cast copper is represented in copper colour, annealed copper in red, and the matrix region compound material in turquoise.

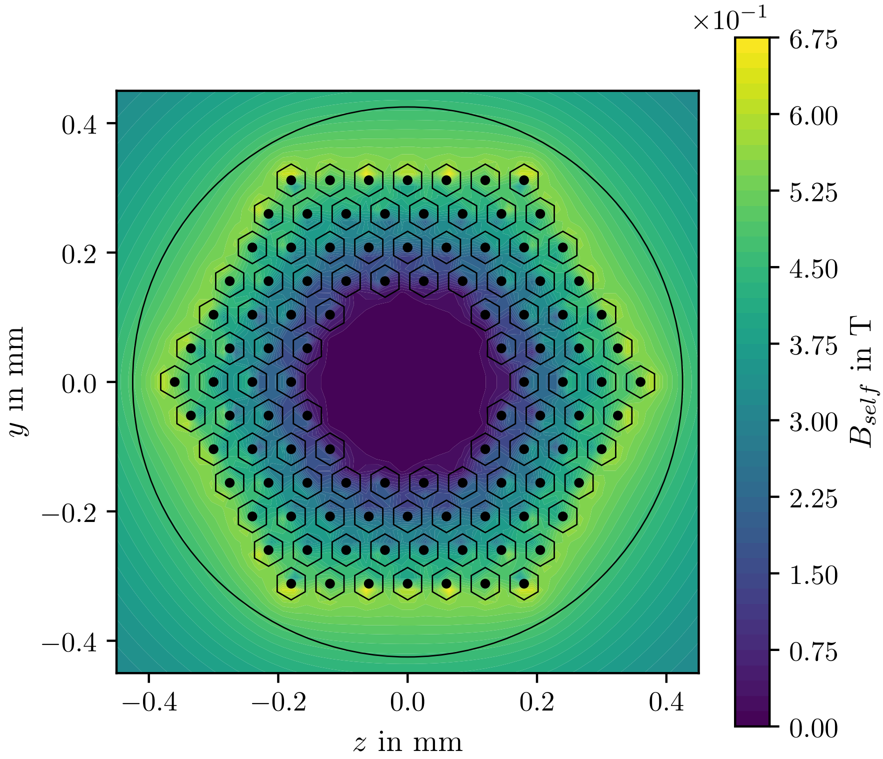

Figure A.6: Self field as calculated for a fully functional strand with a regular mesh at $I_{\text{strand}} = 1\,\text{kA}$

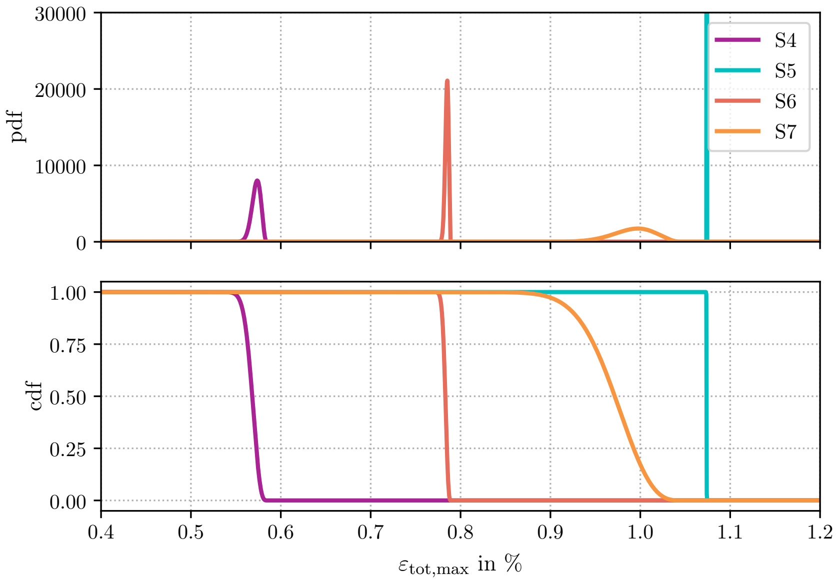

Figure A.7: Visual representation of the distributions defined by the data in Tab.6.2 for relevant samples.
Sample 5 is highlighted in turquoise, because it breaches continuity in hotspot temperature dependence. This is due to the large degradation Sample 5 experiences due to residual strain and how the algorithm finds the respective ε_{irr}. Because, the calculated I_c values for Sample 5 are already well in agreement with the measurement data, any further degradation(which due to the mathematical implementation will occur for reasonable ε_{irr} values) will lead to a worse result. Thus the result from optimisation is well above a reasonable value.

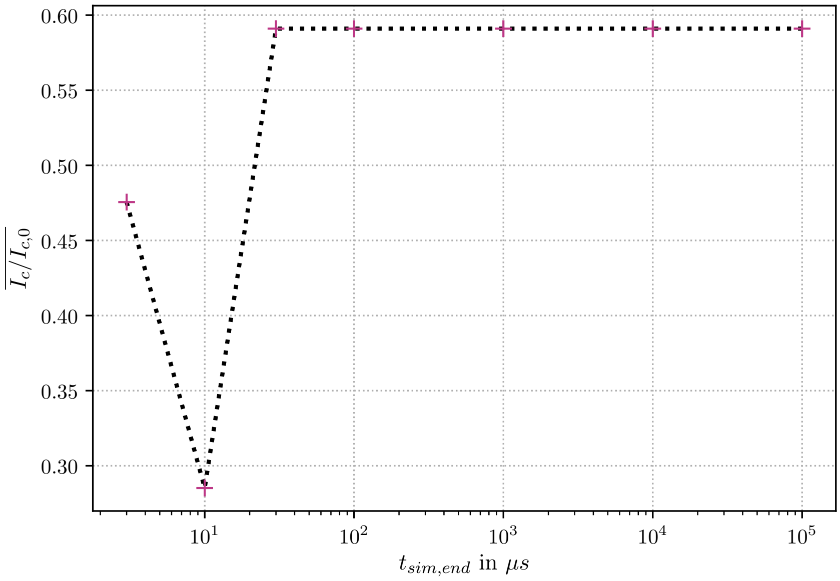

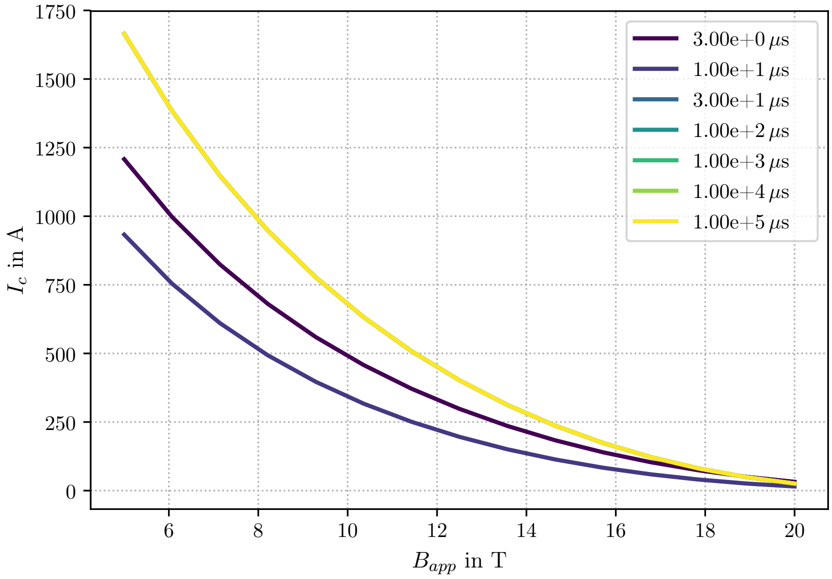

Figure A.8: S5 I_c-degradation calculated with only strain scaling relative to the reference undegraded $I_{c,0}$ curve. The values shown are the average of values calculated for a magnetic field range of 5...20 T, and shown as a function of the total simulated time of the mechanical simulation.
The graphs indicate, that the mechanical state stabilises 30 µs after beam impact.

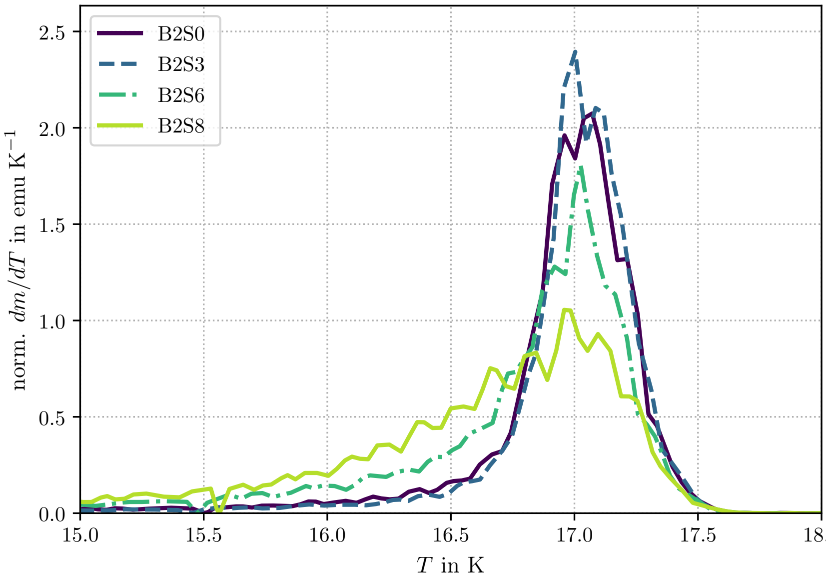

Figure A.9: Non-filtered T_c-density measurement data as derived from magnetic moment measurements. The curves are normalised to an integrated surface of 1 in the given representation.

B Monte Carlo Method

The expectation value of an integrable one dimensional function f evaluated at a random location can be written as:

$$I[f] = \int_0^1 f(x)\mathrm{d}x = \bar{f} \quad . \tag{B.1}$$

In a more general sense we can write for $\boldsymbol{x} \in [0,1]^d$ (this is the d-dimensional unit cube)

$$I[f] = \int_{I^d} f(\boldsymbol{x})\mathrm{d}\boldsymbol{x} =: E[f(\boldsymbol{x})] \quad . \tag{B.2}$$

Let now $\{\boldsymbol{x}_\mathrm{n}\}$ be a sequence sampled from the uniform distribution over the unit cube, then

$$I_N[f] = \frac{1}{N}\sum_{n=1}^{N} f\left(\boldsymbol{x}_n\right) \tag{B.3}$$

and according to the Law of Large Numbers

$$\lim_{N\to\infty} I_N[f] \to I[f] \quad . \tag{B.4}$$

Then the Monte Carlo integration error

$$\epsilon_N[f] = I[f] - I_N[f] \tag{B.5}$$

becomes for large N:

$$\epsilon_N[f] \approx \sigma\nu N^{-1/2} \quad , \tag{B.6}$$

where σ is the square root of the f variance, and ν represents a standard normal random variable.

In other words, for large N and an unbiased choice (this is the case when $E\left[I_\mathrm{N}[f]\right] = I[f]$ for all N) of x_ns, $I_\mathrm{N}[f]$ will converge with the expectation of f.

C Selbstständigkeits- und Nutzungserklärung

Ich erkläre hiermit, dass ich die vorliegende Bachelorarbeit selbständig und nur unter Verwendung der angegebenen Hilfsmittel und Quellen angefertigt habe. Aus fremden Quellen übernommene Gedanken, Werte und Zitate sind als solche deutlich kenntlich gemacht. Die Bachelorarbeit ist an keiner anderen Stelle als Prüfungsleistung verwendet worden oder als Veröffentlichung erschienen. Die eingereichte schriftliche Fassung entspricht der auf dem elektronischen Speichermedium. Seitens des Verfassers bestehen keine Einwände, die vorliegende Bachelorarbeit für die öffentliche Nutzung zur Verfügung zu stellen.

Jena, 9. Juli 2020 Schubert

Jonathan Schubert